

This work was written as part of one of the author's official duties as an Employee of the United States Government and is therefore a work of the United States Government. In accordance with 17 U.S.C. 105, no copyright protection is available for such works under U.S. Law.

Public Domain Mark 1.0

<https://creativecommons.org/publicdomain/mark/1.0/>

Access to this work was provided by the University of Maryland, Baltimore County (UMBC) ScholarWorks@UMBC digital repository on the Maryland Shared Open Access (MD-SOAR) platform.

**Please provide feedback**

Please support the ScholarWorks@UMBC repository by emailing [scholarworks-group@umbc.edu](mailto:scholarworks-group@umbc.edu) and telling us what having access to this work means to you and why it's important to you. Thank you.

# JGR Atmospheres



## RESEARCH ARTICLE

10.1029/2023JD039152

### Key Points:

- Changes of cloud properties and radiative fluxes by cloud type with degree of convective aggregation are examined with CERES observations
- Results using four convective aggregation indices are largely similar except for optically thick and low-level clouds from two indices
- Changes of cloud properties and radiative fluxes by cloud type are primarily related to changes in degree of convective aggregation

### Correspondence to:

K.-M. Xu,  
Kuan-Man.Xu@nasa.gov

### Citation:

Xu, K.-M., Zhou, Y., Sun, M., Kato, S., & Hu, Y. (2023). Observed cloud type-sorted cloud property and radiative flux changes with the degree of convective aggregation from CERES data. *Journal of Geophysical Research: Atmospheres*, 128, e2023JD039152. <https://doi.org/10.1029/2023JD039152>

Received 24 APR 2023

Accepted 28 AUG 2023

### Author Contributions:

**Conceptualization:** Kuan-Man Xu, Yaping Zhou  
**Data curation:** Kuan-Man Xu, Yaping Zhou, Moguo Sun  
**Formal analysis:** Kuan-Man Xu, Yaping Zhou  
**Funding acquisition:** Kuan-Man Xu, Yaping Zhou  
**Investigation:** Kuan-Man Xu, Yaping Zhou  
**Methodology:** Kuan-Man Xu, Yaping Zhou  
**Project Administration:** Kuan-Man Xu  
**Resources:** Kuan-Man Xu, Yaping Zhou  
**Software:** Kuan-Man Xu, Yaping Zhou  
**Supervision:** Kuan-Man Xu

© 2023 The Authors. This article has been contributed to by U.S. Government employees and their work is in the public domain in the USA.

This is an open access article under the terms of the [Creative Commons Attribution License](#), which permits use, distribution and reproduction in any medium, provided the original work is properly cited.

## Observed Cloud Type-Sorted Cloud Property and Radiative Flux Changes With the Degree of Convective Aggregation From CERES Data

Kuan-Man Xu<sup>1</sup> , Yaping Zhou<sup>2</sup> , Moguo Sun<sup>3</sup>, Seiji Kato<sup>1</sup>, and Yongxiang Hu<sup>1</sup> 

<sup>1</sup>NASA Langley Research Center, Hampton, VA, USA, <sup>2</sup>University of Maryland Baltimore County/NASA Goddard Research Center, Greenbelt, MD, USA, <sup>3</sup>Science Systems and Applications Inc./NASA Langley Research Center, Hampton, VA, USA

**Abstract** Cloud-radiation interactions are a critical mechanism for convective self-aggregation, especially the longwave radiative cooling of low clouds and environments. In this study, two data products from CERES observations combined with MERRA-2 reanalysis are used to understand the changes of cloud properties and radiative fluxes by cloud type with the degree of convective aggregation at the 1000-km scale, which is represented by the number of cloud objects ( $N$ ), simple convective aggregation index (SCAI), modified SCAI (MCAI) or convective organization potential (COP). The changes with SCAI are similar to those with  $N$  as an index, agreeing with previous studies using grid-averaged properties. For changes from weak to strong degrees of aggregation using  $N$  and SCAI, area fractions of middle- and high-level cloud types decrease by up to 4% but those of low-level cloud types increase by up to 2%, and more infrared radiation is emitted to space ( $2\text{--}8\text{ W m}^{-2}$ ) from optically thin cloud types but more solar radiation is reflected ( $2\text{--}4\text{ W m}^{-2}$ ) from optically-thick cloud types. However, using COP (MCAI to lesser extent), area fractions of optically-thick cloud types increase, which emit less infrared radiation and reflect more solar radiation, whereas the area fractions of low-level clouds decrease. These results can be explained by greater expansion of cloud object sizes for COP than MCAI/SCAI as the degree of convective aggregation increases, which also explains the difference between SCAI and MCAI pertaining to the opposite changes of optically-thick high-level clouds. These results can have implications for understanding convective self-aggregation.

**Plain Language Summary** Rainstorms are often clustered in ways that depend upon meteorological conditions; this is known as “convective aggregation.” The amount of aggregation has a large influence on both weather and climate, so being able to understand how the properties of rainstorms change with the strength of convective aggregation is important for weather and climate modeling. Previous studies used satellite data that only characterized the cold and deep parts of rainstorms. This study provides an analysis of 42 cloud types using the latest satellite data. We assess the changes of cloud area coverage, solar radiation and thermal radiation between two subgroups of data samples with vastly different strengths of aggregation. We find that two of four aggregation measures produce nearly identical changes for cloud area coverages of low- and high-level cloud types, thermal radiation from optically thin cloud types and solar radiation from optically thick cloud types. The other two measures have some differences in how optically-thick cloud types change with aggregation, which are explained by more rapidly-increasing size of rainstorms as the degree of aggregation increases. One of these two measures has the opposite trends in how the low-level cloud area coverages change, which are inconsistent with the other three measures.

## 1. Introduction

Convective aggregation can increase the degree of convective organization from scattered convection that has a horizontal scale of kilometers to mesoscale organization or even larger scales (Mapes, 1993). It includes a mode of self-aggregation phenomenon appearing in idealized radiative-convective equilibrium (RCE) simulations from cloud resolving models (CRMs) and general circulation models (GCMs) under constant, uniform sea surface temperature (SST). A moist cloudy region with intensive deep convective clouds coexists with and is surrounded by an extremely dry subsidence region in the model domain. Due to the lack of external forcing under the RCE setting, the internal feedbacks of convection with its environment are responsible for this convective self-aggregation (CSA) phenomenon (e.g., Bretherton et al., 2005; Held et al., 1993; Muller & Bony, 2015; Muller et al., 2022; Muller & Held, 2012; Wing & Emanuel, 2014; Wing et al., 2017). The general consensus

**Validation:** Kuan-Man Xu, Yaping Zhou

**Visualization:** Kuan-Man Xu, Yaping Zhou

**Writing – original draft:** Kuan-Man Xu

**Writing – review & editing:** Kuan-Man Xu, Yaping Zhou, Moguo Sun, Seiji Kato, Yongxiang Hu

on the physical mechanisms for CSA is that radiative feedbacks are particularly important in addition to moisture feedbacks. The onset and maintenance of CSA may be operated by different mechanisms. For onset, the longwave cooling near the top of low clouds in dry and subsiding regions force a shallow circulation between the boundary-layer top ( $\sim 500$  m) and low cloud top (below  $\sim 2$  km) that induces upgradient energy transports and radiative-convective instability. Once the CSA and its associated deep circulation between moist and dry regions are established, the strong clear-sky radiative cooling in the dry region and heating in the cloudy regions due to high clouds play a major role in maintaining the CSA (Muller & Bony, 2015; Muller & Held, 2012; Pope et al., 2021) while cloud-radiative interactions of low clouds play a complementary role to that of high level clouds. In addition, shortwave radiative heating and cool pools tend to weaken CSA while surface fluxes tend to strengthen CSA at the initial stage but weaken CSA at the later stage. The relative roles of these mechanisms are uncertain due to their sensitivities to numerical setups such as the domain size of CRMs and their grid resolutions, as well as the physical parameterizations used in GCMs.

Observational analyses of convective aggregation (e.g., Bony et al., 2020; Masunaga et al., 2021; Stein et al., 2017; Tobin et al., 2012, 2013) have been performed to identify relationships between atmospheric variables and measures of convective aggregation. Tobin et al. (2012) found that  $10^\circ \times 10^\circ$  [or  $3^\circ \times 3^\circ$  in Tobin et al. (2013)] averaged column water vapor/relative humidity (RH) and middle-to-upper tropospheric RH are lower while outgoing longwave radiation (OLR) is higher ( $\sim 20$  W  $\text{m}^{-2}$  from the least to most aggregated states) and albedo is lower ( $\sim 0.05$  or  $\sim 20$  W  $\text{m}^{-2}$  in terms of shortwave flux) for aggregated convection, compared to non-aggregated convection. These results are qualitatively consistent with RCE simulations. An increase in low-level cloud cover with increased aggregation is also noticed in Tobin et al. (2013), Lebsock et al. (2017), and Stein et al. (2017) while a contraction in high-level anvil clouds is pronounced (Tobin et al., 2012, 2013), which are typically associated with deep cumulus towers (Stein et al., 2017). The reduced low-level clouds with aggregation noticed in Tobin et al. (2012) may be due to very coarse resolution of satellite data used, compared to that of other studies (Masunaga et al., 2021; Stein et al., 2017; Tobin et al., 2013). The top-of-the-atmosphere (TOA) net radiation budget related to reduced high-level cloudiness and surface turbulent fluxes are not as sensitive to aggregation as that found in RCE simulations (Tobin et al., 2012). Masugana et al. (2021) analyzed the short-term transient behaviors of convective aggregation and its related mechanisms and they found that the sign of transient aggregation is only evident for heavy precipitation and high SST regimes.

Convective aggregation can occur under a variety of external forcings and spatial scales in reality (e.g., Nakazawa, 1988; Zeng, 2023) while CSA occurs without any external forcing, that is, under the RCE. The identified relationships of atmospheric variables with the degree of convective aggregation in the aforementioned studies were obtained by restricting the characteristics associated with external forcing factors such as sea surface temperature, precipitation and large-scale ascent, as well as the diurnal cycle. Even with these restrictions, these relationships can still be influenced by external forcing factors, for example, the spatial inhomogeneity of SST within the analysis grid box. Furthermore, the tropical atmosphere is hardly under the RCE (Jakob et al., 2019), which is one of the obstacles for comparing the observed convective aggregation at much larger spatial scales (Mapes, 1993) with CSA.

Several different indices of convective aggregation have been proposed for observational analyses (Kadoya & Masunaga, 2018; Tobin et al., 2012; White et al., 2018; Xu et al., 2019) and modeling studies (e.g., Bao et al., 2017; Bretherton et al., 2005; Tompkins & Semie, 2017). The former is typically based upon cloud morphology using the number of clouds and the distances among the clouds (Tobin et al., 2012; Tompkins & Semie, 2017; White et al., 2018; Xu et al., 2019). The latter is based upon the moisture and dynamic aggregation such as the mean and horizontal variances of moist static energy and precipitable water and the subsidence/ascending fractions (e.g., Arnold & Randall, 2015; Bao et al., 2017; Bretherton et al., 2005; Coppin & Bony, 2015) except for the organization index (Tompkins & Semie, 2017). Because each of the indices used in observational and modeling studies measures a different aspect of convective aggregation (e.g., Bao et al., 2017), intercomparison of convective aggregation indices may help to understand their behaviors and address to what extent CSA is relevant to convective aggregation in nature (Holloway et al., 2017; Lebsock et al., 2017; Masunaga et al., 2021).

As mentioned above, the inferred relationships of observed atmospheric properties with the degree of convective aggregation are focused upon the area-averaged properties, which include the contributions from both the clear and cloudy regions and are determined by the relative fraction of clear (or cloudy) regions due to large contrasts in the properties between the two regions. For example, the clear-sky albedo over ocean can be as low as 0.1 but

the cloudy sky albedo can vary greatly, depending upon the cloud types, and it can be higher than 0.8. In previous studies (Tobin et al., 2012, 2013; Bony et al., 2020; Masunaga et al., 2021), except for Stein et al. (2017) using active-sensor observations of different cloud types, however, cloudy regions were defined as those satellite pixels with the infrared (10–12.5  $\mu\text{m}$ ) brightness temperature ( $T_b$ ) less than 240 K while pixels warmer than 240 K were treated as the environment of deep convection. This definition of the environment compounds of the truly clear regions and the cloudy regions with warmer and optically thin high-level cloud types while the cloudy regions consist of high-level clouds only with a narrow range of optical thicknesses such as cirrostratus and deep convective cores. Even for these two types of clouds, both albedo and infrared emissivity can vary greatly. Therefore, it is necessary to obtain the properties and their changes with the degree of convective aggregation for as many cloud types as possible in a grid box, instead of the mean cloud properties. Such an approach is made possible with the International Satellite Cloud Climatology Project (ISCCP), which classifies cloudy satellite pixels into 42 cloud types, consisting of seven cloud top pressure ( $p_c$ ) bins and six cloud optical depth ( $\tau$ ) bins, plus the truly clear area (Rossow & Schiffer, 1999). Differing from the ISCCP approach, the FluxByCldTyp (FBCT) data product from the Clouds and Earth's Radiant Energy System (CERES) observations (Eitzen et al., 2017; Sun et al., 2022) provides the mean cloud properties and radiative fluxes for each cloud type over  $1^\circ \times 1^\circ$  grids, in addition to the frequency of occurrence. In conjunction with another CERES data product, that is, single satellite footprint (SSF), which has been used to produce deep convective cloud objects (Xu et al., 2005, 2007, 2008, 2016, 2017) and compute morphology-based convective aggregation indices (Xu et al., 2019), this study can take advantage of these data products to further understand the relationships of cloud and radiative properties with the degree of convective aggregation at the 1,000-km scale, as in Tobin et al. (2012) and Stein et al. (2017).

The objective of this study is to provide an observational understanding of convective aggregation, particularly, the sensitivity of cloud properties and radiative fluxes by cloud type to the degree of convective aggregation at the 1,000-km scale. We will emphasize the changes of cloud properties and radiative fluxes between two strengths of convective aggregation. Our approach will rely less upon the restrictions on the external forcing factors than in the earlier studies (e.g., Tobin et al., 2012, 2013) as long as the probability distributions of external forcing factors are similar between two subsets of data that are compared against each other. This deemphasis on the external forcing factors associated with individual aggregation states will hopefully lead to a better comparison of the results with the CSA. The results will be also useful for the CSA community because analyses of CRM-simulated CSA characteristics according to cloud types are emerging (Pope et al., 2021, 2023).

The rest of this paper is organized as follows. The data sets used, convective aggregation indices and detailed methodology of the analyses are described in Section 2. Results of the analyses will be presented in Section 3. Summary and conclusions will be given in Section 4.

## 2. Data Sets and Analysis Methodology

### 2.1. Satellite and MERRA-2 Reanalysis Data

Two different CERES data products are used in this study. The first one, the level-2 CERES single satellite footprint (SSF) data product, was used to generate cloud objects (Xu et al., 2005), whose information was used to calculate convective aggregation indices (Xu et al., 2019). Each SSF file contains 1 hr of instantaneous satellite measurements. SSF contains cloud optical and micro- and macro-physical properties retrieved using multispectral data from the Moderate Resolution Imaging Spectrometer (MODIS), as well as broadband TOA reflected shortwave (SW) and emitted longwave (LW) fluxes from the CERES scanner. The average CERES footprint size on Aqua is approximately  $20 \times 20 \text{ km}^2$ , while the MODIS pixel data used in retrieval cover an area of  $2 \times 2 \text{ km}^2$ . The retrieved cloud properties are averaged over the larger CERES footprint based upon a point spread function that gives more weighting to the pixels near the center of the footprint (Green & Wielicki, 1997). The details about the cloud retrieval algorithm and the CERES radiative fluxes can be found in Minnis et al. (2011, 2020) and Loeb et al. (2003), respectively.

The methodology for generating cloud objects was described in Xu et al. (2005, 2007, 2008, 2015). Briefly, it groups the contiguous deep convective footprints into an object, which is parts of a convective aggregate. The shape and size of cloud objects are determined by both the satellite data and the selection criteria of convective objects. The selection criteria consist of (a) a footprint being overcast, (b) cloud top pressure being less than 440 hPa ( $\sim 10 \text{ km}$  in the Tropics), and (c) cloud optical depth (COD) being greater than 10. The last two criteria

capture most parts of a deep convective system, but exclude adjacent optically thin anvils and shallow clouds. The first criterion excludes small clouds (<20 km in diameter) and scattered convection from a cloud object. But cloud and radiative properties for undetected cloud objects that are smaller than 75 km in equivalent diameter (not saved in database) and adjacent footprints for shallow, optically thin or small clouds are contained in the FBCT data to be introduced later.

The second CERES data product is FluxByCldTyp (FBCT), which provides either combined or separated Terra and Aqua daily daytime-averaged cloud properties and radiative fluxes stratified by effective cloud (“radiating” top) pressure ( $p_c$ ) and cloud optical depth ( $\tau$ ) bins (Eitzen et al., 2017; Sun et al., 2022). That is, the  $p_c - \tau$  pair describes a cloud type with the MODIS pixel ( $2 \times 2$  km<sup>2</sup>) data. There are seven  $p_c$  bins and six  $\tau$  bins, that is, 42 cloud types, plus a cloud-free bin, following the ISCCP definition of cloud types (Rossow & Schiffer, 1999). Cloud microphysical and macrophysical properties of these cloud types are directly from the CERES cloud retrieval (Minnis et al., 2011, 2020). The algorithm for obtaining cloud type-sorted radiative fluxes was developed following these steps: (a) computing subfootprint broadband radiances for the clear-sky and cloudy portions of the CERES footprint from the MODIS narrowband channel radiances based on empirically derived narrowband to broadband coefficients, where a footprint may contain up to three non-overlapping subfootprints: low and high cloud layers and clear area, (b) converting the mean broadband radiances to the subfootprint fluxes using the CERES angular distribution models (ADMs), (c) verifying the combined subfootprint fluxes with the “observed” footprint flux (Loeb et al., 2003), which is used to normalize the subfootprint fluxes, and (d) assigning each of the single-scene footprints and subfootprint cloud layers to  $p_c - \tau$  cloud types and obtaining the cloud-type averaged fluxes for  $1^\circ \times 1^\circ$  grid that are weighted by the areal extents of single-scene footprints and subfootprint cloud layers. Instantaneous shortwave fluxes are converted to equivalent daily-mean fluxes by the method explained in Sun et al. (2022).

The Aqua FBCT, which is currently available from July 2002 to late 2022, instead of the combined Terra and Aqua FBCT, is used to ensure consistency with the cloud object data. Other variables include solar insolation, clear sky SW and LW fluxes and TOA albedo, which is calculated from the ratio of SW flux to solar insolation. The original  $1^\circ \times 1^\circ$  grid data are aggregated onto  $10^\circ \times 10^\circ$  grids when being matched with the convective aggregation index data in space and time (see Section 2.2).

The Modern-Era Retrospective Analysis for Research and Applications, Version 2 (MERRA-2) is an atmospheric reanalysis of the modern satellite era, using the Goddard Earth Observing System Model (Rienecker et al., 2011), Version 5 (GEOS-5) data assimilation system, Version 5.12.4 (Gelaro et al., 2017). MERRA-2 spans the period from 1980 to the present. Modern hyperspectral radiance and microwave observations, along with Global Positioning System (GPS) Radio Occultation and NASA ozone datasets are assimilated in MERRA-2. The model used for the reanalysis has a horizontal grid spacing of  $0.625^\circ$  (longitude) by  $0.5^\circ$  (latitude), and the native vertical grid of 72 pressure levels from 1,000 to 0.1 hPa, with a 25 hPa interval below 700 hPa. The data are output at an hourly interval.

For this study, only the pressure vertical velocity at 500 hPa ( $w_{500}$ ) and surface precipitation rate data from MERRA-2 averaged horizontally to a  $10^\circ \times 10^\circ$  grid and accumulated in time over a 1-day period will be used, which are matched with the CERES data products in space and time (within  $\pm 12$  hr). The CERES data products provide snapshots of cloud systems at various times of the day with high spatial-resolution ( $2 \text{ km} \times 2 \text{ km}$ ) observations of cloud and radiative properties. The degree of convective aggregation thus represents that of a snapshot of cloud systems at the 1,000-km scale. The lack of temporal resolution is a major limitation of polar-orbiting satellites such as Aqua satellite used in this study compared to geostationary satellites.

## 2.2. Convective Aggregation Indices

Three cloud-morphology aggregation indices will be used in this study, in addition to the number of cloud objects ( $N$ ) per day within a  $10^\circ \times 10^\circ$  grid. Only cloud objects with equivalent diameters greater than 75 km were used in computing these indices because smaller ones were not saved (Xu et al., 2005, 2019). These indices are designed to be a metric of convective clustering or clumping (e.g., Tobin et al., 2012; Xu et al., 2019). The simple convective aggregation index (SCAI), as proposed by Tobin et al. (2012), measures the clumping of clouds within a region using satellite brightness temperature data (at 50-km spacing). It is proportional to normalized number of clouds and distance between them. The distance between a pair of clouds is computed from the centroids of



clouds. Xu et al. (2019) modified this index by computing the distance between “equivalent” circumferences of two clouds, instead of from their centroids as used in SCAI. This modified SCAI, hereafter, MCAI, captures the physical closeness of clouds. Obviously, the value of MCAI is smaller than that of SCAI, but both have the same dependency on normalized numbers of clouds. White et al. (2018) used the ratio of the sum of radii of clouds to the distance between a pair of clouds to define an organization potential metric called convective organization potential (COP), which measures the average interaction potential among clouds, meaning that small clouds have less interaction potential than large clouds if the distance between them is the same. The number of clouds is not explicitly used in COP except for summation of the ratios (organization potentials) between different pairs of clouds. MCAI was shown to capture some behaviors of COP but similar to SCAI in other aspects according to the results shown in Xu et al. (2019). Note that a higher SCAI/MCAI value corresponds to a lower degree of aggregation; hence SCAI/MCAI actually measures the degree of disaggregation. However, a higher value of COP corresponds to a higher degree of organization.

Figure 1 shows density-scatter plots among the three indices using a subset of the same data set as in Xu et al. (2019) for the oceanic regions with restrictions on  $\omega_{500}$  and surface rainfall rates (Table 1). The results are consistent with the conclusion drawn in Xu et al. (2019). The strongly aggregated states as measured by small values of MCAI and SCAI (Figure 1c) are matched very well. The strongly aggregated states as measured by MCAI and COP (Figure 1b) are more closely matched in terms of small spreads for a given value of COP, compared to those by SCAI versus COP (Figure 1a). MCAI is more closely related to COP than SCAI is despite of the strong correlation between SCAI and MCAI (Figure 1c).

### 2.3. Analysis Methodology

The cloud object data as described in Xu et al. (2005) are available over the region between 25°S and 25°N for a 4-year period between July 2006 and June 2010. The number of cloud objects, their radii and adjacent distances (either from centroids or circumferences) within a  $10^\circ \times 10^\circ$  grid are used to calculate the three convective aggregation indices (Xu et al., 2019). Note that SCAI, MCAI and COP values are undefined based upon the respective formula when there is a single cloud object within a  $10^\circ \times 10^\circ$  grid. Theoretically, these single objects should be treated as being the most aggregated ones with SCAI/MCAI being 0 and COP being 1, respectively. However, the actual SCAI/MCAI (COP) values are larger (smaller) than these theoretical ones if one takes into account the unavailable, small cloud objects (with equivalent diameters less than 75 km) in a  $10^\circ \times 10^\circ$  grid. This is particularly true for the earlier stages of convective self-aggregation when many small convective cells are present. See Xu et al. (2019) for further details and discussions of these indices.

In previous observationally-based studies of convective aggregation, Tobin et al. (2012, 2013) and Stein et al. (2017) have stratified data according to various factors, such as precipitation regimes, sea surface temperature (SST) bins, and the number of clusters ( $N$ )/SCAI, as well as the large-scale dynamics. Since we are only interested in convective aggregation over the tropical oceanic regions, we first eliminate the land grids using land fraction being greater than 67%. This results in reductions of data sample sizes from 36,079 to 25,985 (or 28%) for single cloud object grids and from 30,912 to 20,235 (or 34%) for multiple cloud object grids, respectively (Table 1). We also eliminate the grids with extremely strong large-scale forcings with  $10^\circ \times 10^\circ$  grid-averaged  $|\omega_{500}| > 0.1 \text{ Pa s}^{-1}$ . This mainly affects the grids associated with strong large-scale ascents. This procedure results in further reductions of data sample sizes from 25,985 to 22,786 (or 12%) for single cloud object grids and from 20,235 to 15,908 (or 21%) for multiple cloud object grids, respectively (Table 1), indicating stronger large-scale forcings for multiple cloud object grids, which can be seen from histograms of  $\omega_{500}$  (pressure velocity at 500 hPa) for different  $N$  subgroups shown later. In addition, we isolated two narrow  $\omega_{500}$  bins (regimes) with  $|\omega_{500}| < 0.01 \text{ Pa s}^{-1}$  (W0) and  $-0.03 < \omega_{500} \leq -0.01 \text{ Pa s}^{-1}$  (W2), each consisting of roughly one-fifth of the data samples of the  $|\omega_{500}| < 0.1 \text{ Pa s}^{-1}$  ( $W_{\text{all}}$ ) regime with  $10^\circ \times 10^\circ$  grid-mean precipitation greater than  $2.39 \text{ mm day}^{-1}$  (see Table 1). The reason for excluding grids with precipitation less than  $2.39 \text{ mm day}^{-1}$  will be discussed later. The first narrow  $\omega_{500}$  bin (W0) is designed to mimic the RCE states while the second  $\omega_{500}$  bin (W2) represents a stronger influence of large-scale ascent on the convective organization than the first  $\omega_{500}$  bin. We do not further stratify the data according to the SST regimes, which will be justified in Section 3.4.

Regarding the precipitation regimes, Tobin et al. (2012, 2013) noticed similar results of the dependency on the degree of aggregation for different bin sizes of precipitation regimes. We show PDFs of water vapor mixing ratio at 850 hPa ( $q_{850}$ ), SST, precipitation rate and  $\omega_{500}$  for five quintiles of  $10^\circ \times 10^\circ$  grid-mean surface

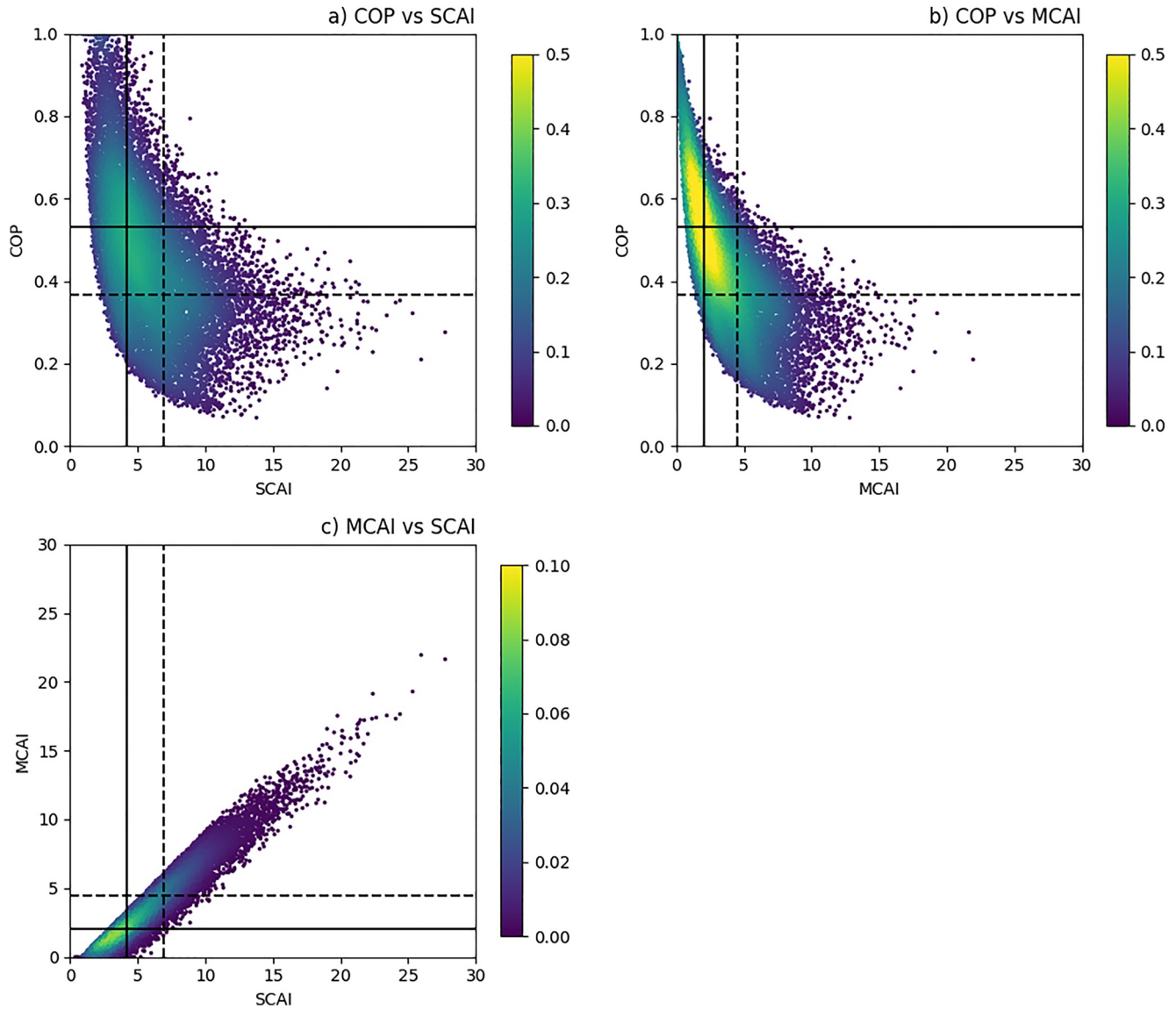


**Figure 1.** Scatterplots of (a) convective organization potential (COP) versus simple convective aggregation index (SCAI), (b) COP versus modified SCAI (MCAI) and (c) MCAI versus SCAI. Solid lines (SCAI = 4.2, MCAI = 2.04, COP = 0.53) demarcate the moderate and strong aggregation terciles while dashed lines (SCAI = 6.94, MCAI = 4.49, COP = 0.366) demarcate the weak and moderate aggregation terciles.

**Table 1**

Number of  $10^\circ \times 10^\circ$  Grids With Single ( $N = 1$ ), Multiple ( $N \geq 2$ ), Two ( $N = 2$ ), Three ( $N = 3$ ) and Four and More ( $N = 4^+$ ) Cloud Objects, Which Are Further Stratified According to Oceanic Grids (all Rows Except for the Row Labeled “Ocean + Lands”), Grid-Mean Pressure Velocity at 500 hPa ( $\omega_{500}$ ), and Surface Precipitation Rate (RR) as Indicated in the First Column

	Single objects	Multiple objects	$N = 2$	$N = 3$	$N = 4^+$	Total
Ocean + lands	36,078	30,912	16,711	8,016	6,185	66,990
Ocean only	25,985	20,235	11,450	5,228	3,557	46,220
Ocean, $ \omega_{500}  < 0.1 \text{ Pa s}^{-1}$	22,786	15,908	9,375	4,058	2,475	38,694
Ocean, $ \omega_{500}  < 0.1 \text{ Pa s}^{-1}$ & $\text{RR} > 2.39 \text{ mm day}^{-1}$	16,978	13,974	7,982	3,653	2,339	30,952
Ocean, $-0.03 < \omega_{500} \leq -0.01 \text{ Pa s}^{-1}$ & $\text{RR} > 2.39 \text{ mm day}^{-1}$	3,252	2,552	1,480	674	398	5,804
Ocean, $ \omega_{500}  < 0.01 \text{ Pa s}^{-1}$ & $\text{RR} > 2.39 \text{ mm day}^{-1}$	3,584	2,370	1,511	570	289	5,954

Note. See texts for further explanation.

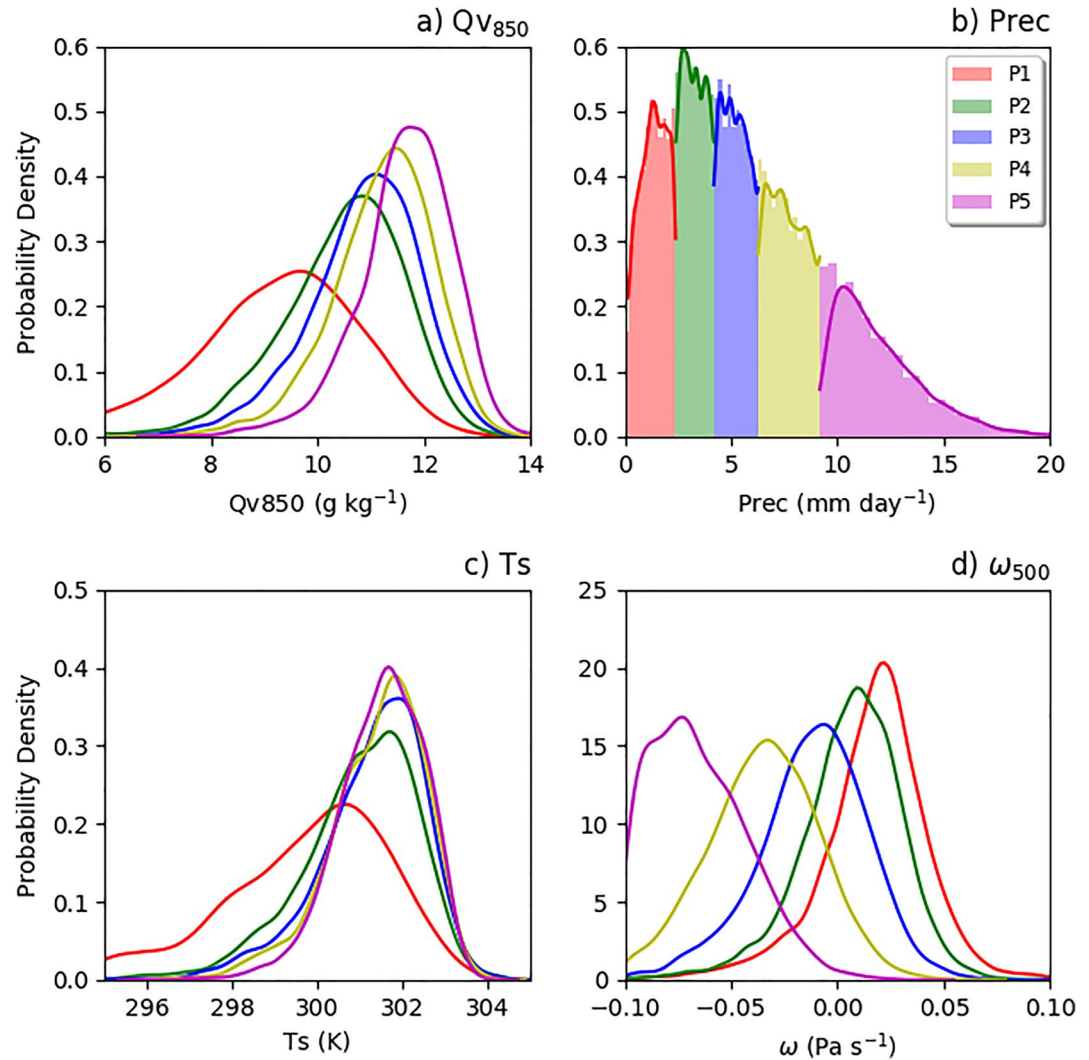


**Figure 2.** Probability density functions of (a) water vapor mixing ratio at 850 hPa, (b) surface precipitation rate, (c) sea surface temperature and (d) pressure vertical velocity at 500 hPa for five quintiles of surface precipitation rates of the single cloud object subset.

precipitation rates of single-object subset in Figure 2. These quintiles are defined as P1 ( $P \leq 2.39 \text{ mm day}^{-1}$ ), P2 ( $2.39 < P \leq 4.19 \text{ mm day}^{-1}$ ), P3 ( $4.19 < P \leq 6.26 \text{ mm day}^{-1}$ ), P4 ( $6.26 < P \leq 9.16 \text{ mm day}^{-1}$ ) and P5 ( $P > 9.16 \text{ mm day}^{-1}$ ). We notice that the atmosphere becomes drier and its large-scale ascent becomes weaker from quintiles 5, 4, 3, 2, to 1. The first quintile stands out with a much drier atmosphere over relatively cooler oceans (i.e., subtropics). Consequently, we excluded this quintile from the rest of the analysis, which further reduces the single-object sample size from 22,786 to 16,978 and multi-object sample size from 20,235 to 13,974. Removing the data samples of P1 regime also substantially reduces the differences in the SST PDFs among the different  $N$ 's subgroups, for example (figure not shown).

As in Tobin et al. (2012, 2013), we start the analysis using the number of cloud objects ( $N$ ) as a simple aggregation index to see the systematic changes of cloud properties and radiative fluxes of different cloud types with  $N$ . For all the dynamic and precipitation (P2-5 or “combined”) regimes, the data sample size is approximately halved as  $N$  increases to the next higher number (Table 1). We further examine the changes by taking the differences in cloud type-sorted cloud properties and radiative fluxes between  $N = 1$  and  $N = 3$  subgroups and between  $N = 2$  and  $N = 4$  and more (4+) subgroups for P2, P3, P4, and combined regimes. This is chosen to examine the differences between two subgroups of data samples with vastly different degrees of convective aggregation. As shown in Xu et al. (2019), there are small overlaps in the histograms of SCAI, MCAI, and COP between  $N = 2$



and  $N = 4^+$  subgroups, but almost none between  $N = 1$  and  $N = 3$  subgroups if one assumes that SCAI/MCAI is 0 (while COP is 1) for the single object grids. Our results confirm that the differences between two  $N$  subgroups (i.e., strong minus weak aggregation) are not sensitive to precipitation regime. Therefore, we will not stratify the data into different precipitation regimes for the later parts of the analyses.

To understand and intercompare how cloud properties and radiative fluxes change with the degree of convective aggregation defined by the three morphology-based indices, we stratify the data into three terciles of SCAI/MCAI/COP and take the differences in cloud type-sorted cloud properties and radiative fluxes between strong and weak aggregation terciles, similar to the analysis using  $N$  as an index. Since SCAI/MCAI/COP indices are not defined for single cloud-object grids, this part of the analysis is only applied to the multiple cloud-object grids with a sample size of 13,974.

To what degree are data samples from the strong (weak) terciles matched with each other since each index measures the degrees of aggregation differently? Figure 1 illustrate the overlaps when both indices indicate strongly aggregated states and mismatches of data samples when one of the indices indicates strongly aggregated states while the other index does not. The strongly aggregated states are defined by those data points in the lower terciles of SCAI (0–4.2) (Figures 1a and 1c) and MCAI (0.0–2.04) (Figures 1b and 1c) but in the upper tercile of COP (0.53–1.0) (Figures 1a and 1b), which are matched at 85% between SCAI and MCAI, 78% between MCAI and COP, but only 63% between SCAI and COP. This is because COP and SCAI are not directly related to each other but both COP and MCAI consider the effect of cloud object sizes (Xu et al., 2019). The weak tercile of COP is matched with the weak terciles of SCAI at 57% and MCAI at 68%, respectively, whereas the weak terciles of SCAI and MCAI are well matched at 88%.

### 3. Results

#### 3.1. Mean Cloud Properties and Radiative Fluxes by Cloud Type

We will first present the mean cloud properties and radiative fluxes by cloud type for the single- and multiple-cloud object subsets, respectively (Figure 3). The mean of the entire data set is the weighted average of the means of these two subsets by their sample sizes (16,978 and 13,974, respectively). This data set excludes the land grids and the oceanic grids with weak precipitation and strong large-scale ascents (Table 1). These mean properties provide a reference for comparing with changes between two subgroups with different degrees of aggregation to be discussed later. For clarity, low-, middle-, and high-level cloud types are defined as those with  $1,000 \geq p_c > 680$  hPa,  $680 \geq p_c > 440$  hPa, and  $p_c \leq 440$  hPa, respectively. A specific  $p_c$  range and/or  $\tau$  range will be given for any other cloud type.

All cloud properties and radiative fluxes are similar between the single- and multi-object subsets, with the exception of cloud area fractions (Figure 3). Cloud fraction for 42 cloud types ranges from <1% to 7.0% for single-object subset (Figure 3a) and from <1% to 9.3% (Figure 3e) for multi-object subset, whereas their respective clear-sky area fractions are 27.8% and 22.8%. The cloud types with less than 0.1% area fractions are drawn with the white color in other panels of Figure 3 (and other figures) to avoid weak statistics. They correspond to the (optically) thickest types with  $1,000 \geq p_c > 310$  hPa and the second thickest types with  $1,000 \geq p_c > 680$  hPa (multi-object subset) or  $1,000 \geq p_c > 800$  hPa (single-object subset). The optically thin-to-thick anvil cloud types with  $310 \geq p_c > 100$  hPa are most prevailing and more abundant in the multi-object subset, with their sum of area fractions being 33.2% in the multi-object subset versus 27.8% in the single-object subset. The optically-thin ( $\tau \leq 9.4$ ) low-level clouds are mostly at 1.0%–4.1% for the multi-object subset but more abundant (1.3%–5.5%) for the single-object subset, which exhibit large relative changes with the degree of aggregation, as shown later.

The mean total cloud liquid and ice water path (TWP) (Figures 3b and 3f) and albedo (Figures 3d and 3h) increase monotonically with the increase of  $\tau$  and the decrease of  $p_c$ . A similar features appears in SW (Figures 3j and 3n). For cloud types with large  $\tau$ , the cloud physical thickness contributes to increasing TWP, albedo and SW as  $p_c$  decreases. Both SW and albedo are affected by factors other than  $\tau$  that result from different cloud microphysical and macrophysical characteristics, such as variation of cloud phase with  $p_c$ . In contrast, the variation of LW with  $p_c$  (Figures 3c and 3g) is similar to that of cloud “effective” (equivalent black body) temperature (Figures 3k and 3o) except for cloud types with small  $\tau$ , which have very small infrared emissivity while optically thick clouds have infrared emissivity close to 1 (Figures 3l and 3p). Infrared emissivity is estimated from  $\tau$ , particle size and cloud and clearsky temperatures (Minnis et al., 1998), but is most sensitive to the variation of  $\tau$  for  $\tau < \sim 30$ .

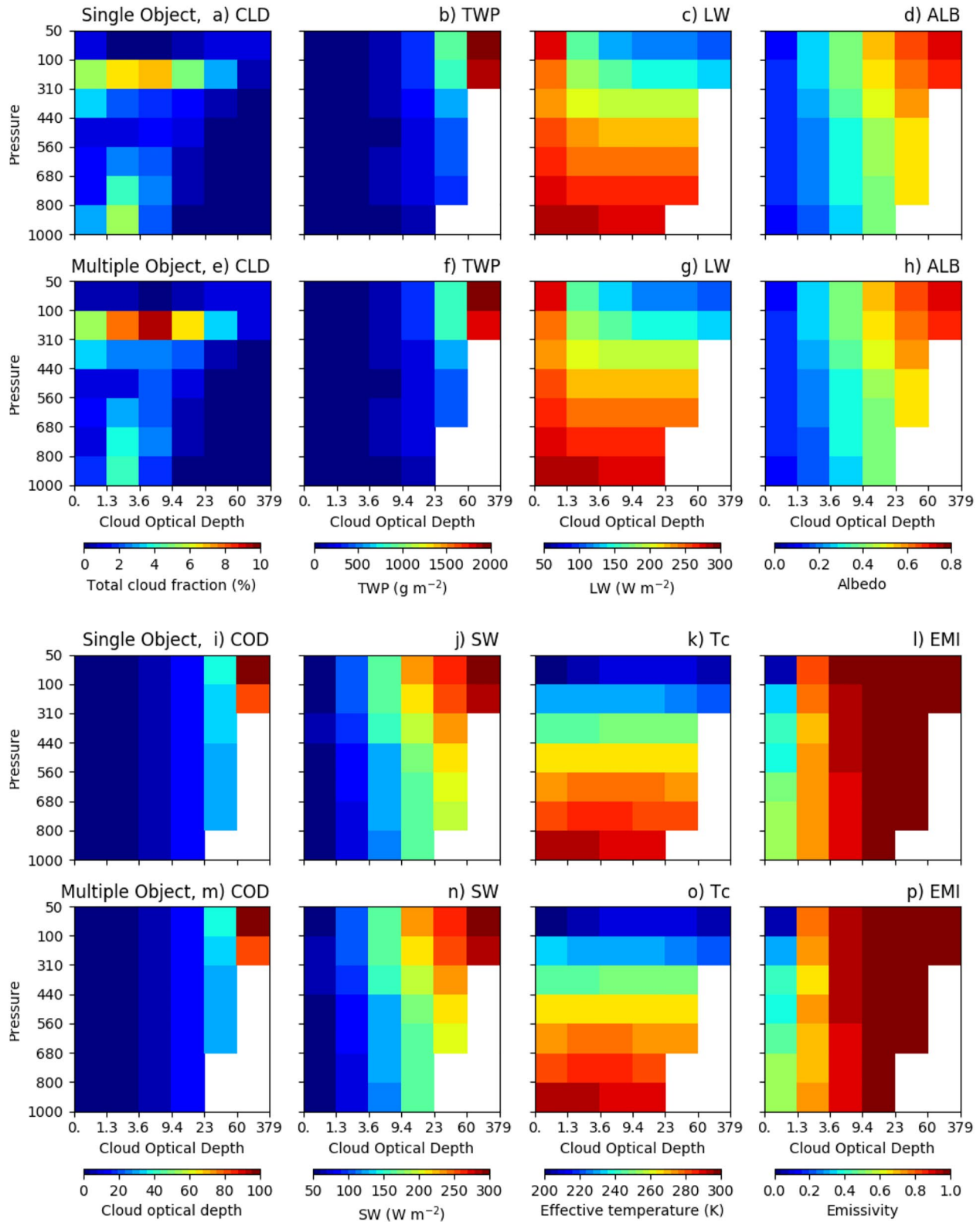


**Figure 3.** The mean cloud area fraction (a), (e), total cloud liquid and ice water path (b), (f), top-of-the-atmosphere (TOA) outgoing longwave flux (c), (g), and TOA albedo (d), (h), cloud optical depth (i), (m), TOA shortwave flux (j), (n), cloud effective temperature (k), (o) and infrared emissivity (l), (p) for  $p_c - \tau$  cloud types of single- (first and third rows) and multi-object (second and fourth rows) subsets.

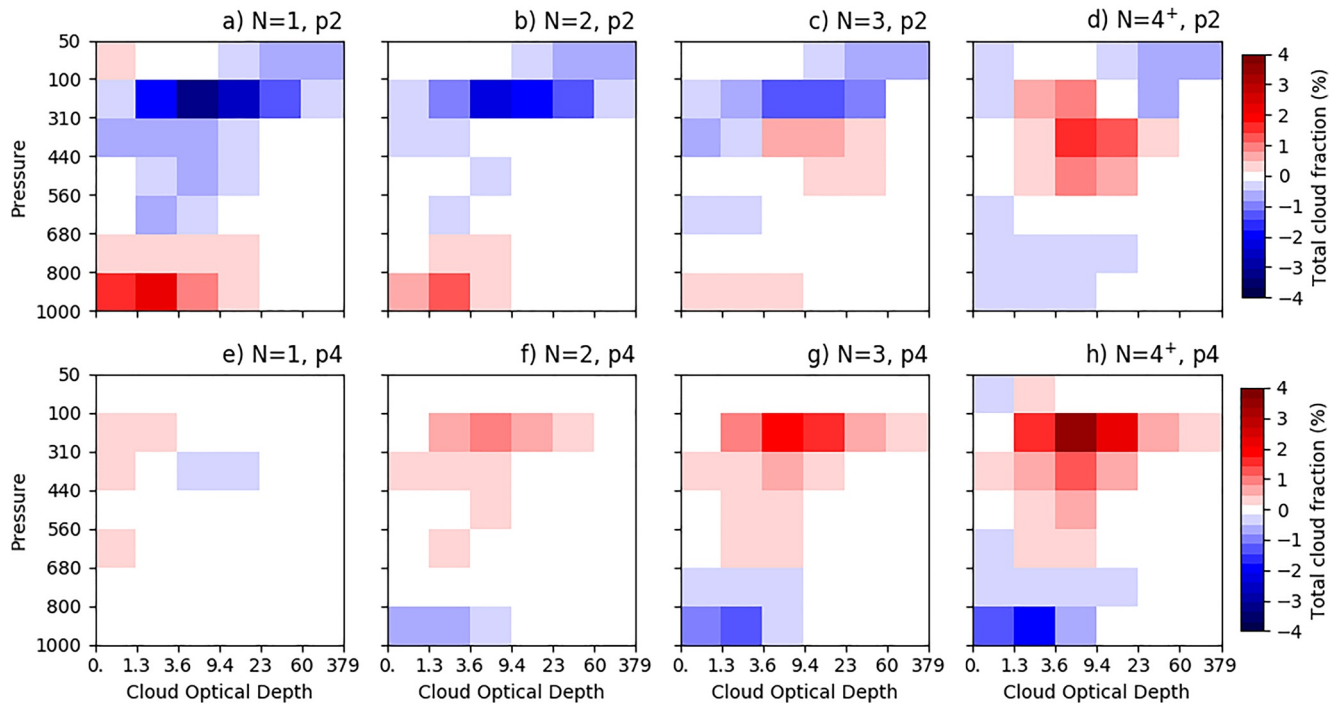


**Figure 4.** The mean cloud area fraction deviations from the entire data set by  $p_c - \tau$  cloud types for the second (top row) and fourth (bottom row) surface precipitation quintiles. Each panel represents a subgroup of data samples with the same number of cloud objects ( $N$ ) within a  $10^\circ \times 10^\circ$  grid box. From left to right, one cloud object (a), (e), two objects (b), (f), three objects (c), (g), and four and more objects (d), (h).

### 3.2. Systematic Changes of Cloud Properties and Radiative Fluxes With $N$

We first present the results of compositing analysis according to the number of cloud objects ( $N$ ). Figure 4 shows the mean cloud area fraction deviations for  $N = 1, 2, 3, 4^+$  subgroups of P2 and P4 precipitation regimes from the mean of the entire (all  $N$ 's) data set (see Figure 3). P2 and P4 are chosen to represent relatively light and heavy precipitation regimes in the Tropics, respectively. The data sample size varies from 5,138, 1,770, 575, to 252, and from 3,920, 2,073, 1,035 to 698 for P2 and P4 regimes as  $N$  increases from 1 to  $4^+$ , respectively (Table 2). The P2 regime has relatively more single-object grids (by  $\sim 25\%$ ) and less multi-object grids than the P4 regime. The large-scale environments of these two precipitation regimes are significantly different. The P2 regime covers a wider range of SST and  $q_{v850}$  variations and has lower SSTs and  $q_{v850}$  than the P4 regime (Figures 5a, 5b, 5e, 5f). The large-scale ascents are also weaker (Figures 5g and 5h). Despite these differences, Figure 4 shows that there are systematic changes with the increase of  $N$  in both regimes: the low-level cloud area fraction decreases by up to 4%, the high-level cloud area fraction increases by up to 6% and the middle-level cloud area fraction

also increases by up to 4% from  $N = 1$  to  $N = 4^+$  subgroups. The clear-sky area fraction decreases with the increase of  $N$ , from 34.9% ( $N = 1$ ) to 23.8% ( $N = 4^+$ ) and from 24.4% ( $N = 1$ ) to 18.2% ( $N = 4^+$ ) for P2 and P4 regimes, respectively. The same systematic increases in low-level clouds of both regimes, also found in Stein et al. (2017), are likely linked to the decrease of deep clouds and the drier middle/upper tropospheric environments, accompanied by increasing clear-sky areas, as  $N$  decreases, suggesting that deep circulation between cloudy and clear regions is strengthened as convective systems are aggregated.

The systematic changes with the increase of  $N$  for high-level clouds, also found by Tobin et al. (2012, 2013) and Stein et al. (2017), may be explained by the differences in anvil areas between connected and separated convective systems. According to Yuan and Houze (2010), anvils of connected convective systems are more extended than those of separated convective systems. Our result agrees to theirs, that is, high-level cloud fractions are larger for

**Table 2**  
Same as Table 1 Except for Further Breaking Down Its Third Row (Ocean,  $|\omega_{500}| < 0.1 \text{ Pa s}^{-1}$ ) by Precipitation Regimes

	Single objects	Multiple objects	$N = 2$	$N = 3$	$N = 4^+$	Total
P1	5,804	1,933	1,392	405	136	7,737
P2	5,138	2,597	1,770	575	252	7,735
P3	4,391	3,345	2,034	865	446	7,736
P4	3,920	3,806	2,073	1,035	698	7,726
P5	3,529	4,226	2,105	1,178	943	7,755
Total (without P1)	16,978	13,974	7,982	3,653	2,339	30,952

Note. Last row of this table is identical to the fourth row of Table 1.

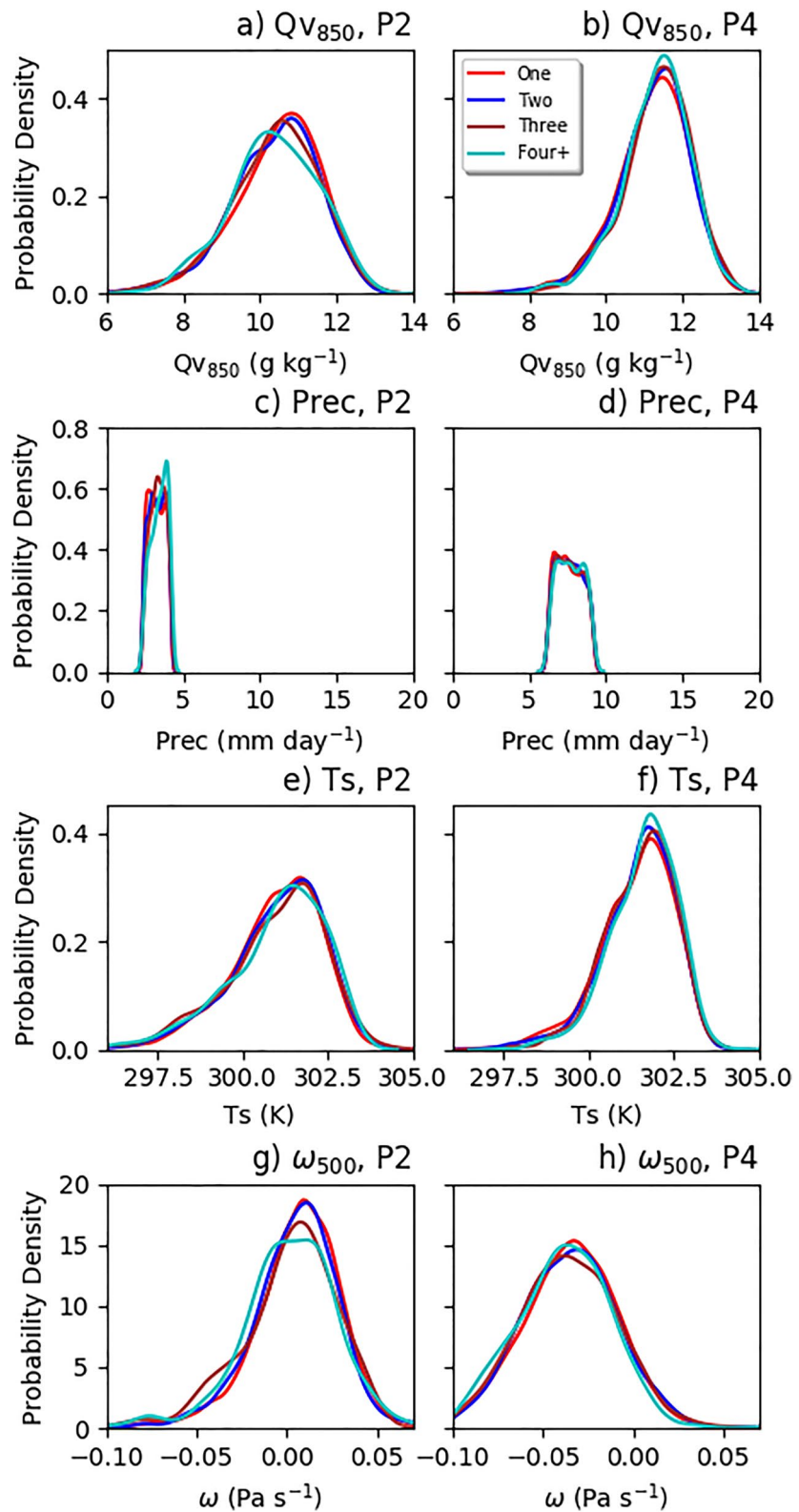


**Figure 5.** As in Figure 2, but for subgroups with one, two, three, or four and plus cloud objects within a  $10^\circ \times 10^\circ$  grid of the P2 and P4 precipitation regimes.

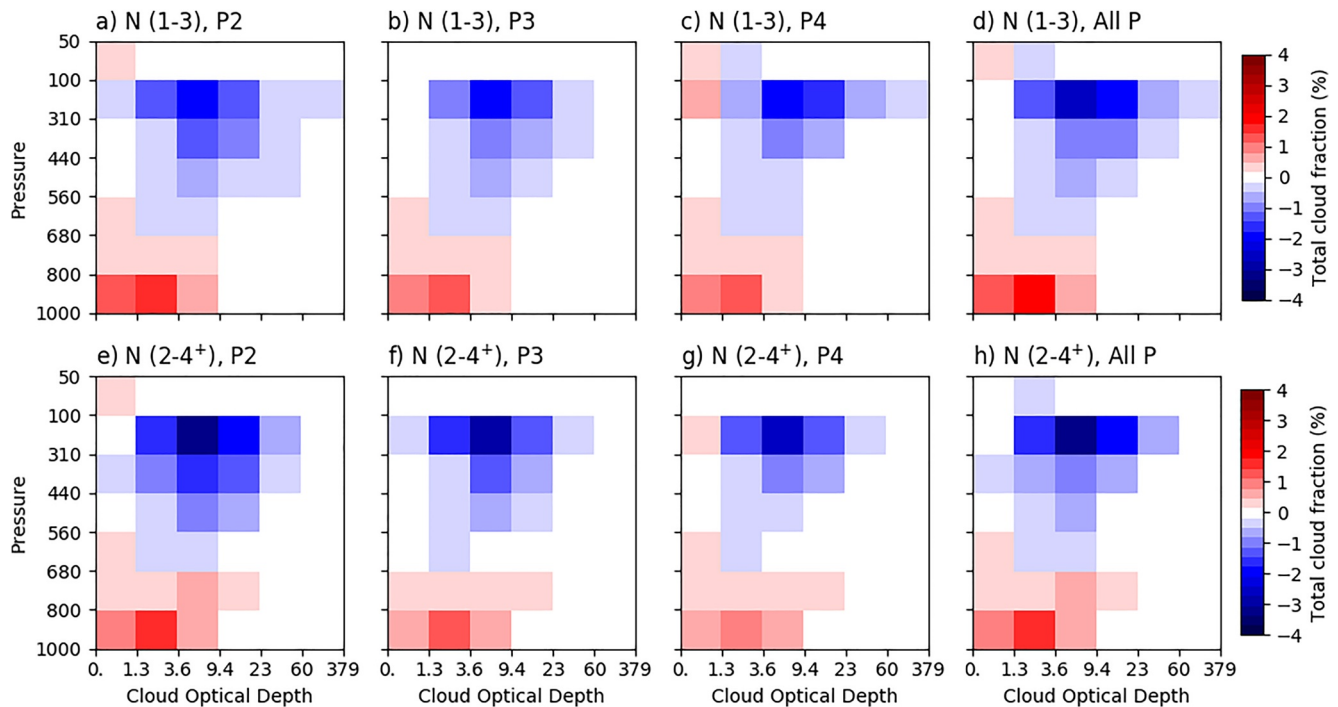


**Figure 6.** The mean differences in cloud area fraction of  $p_c - \tau$  cloud types between subgroups with one and three cloud objects (top row) and between subgroups with two and four and plus (4+) cloud objects (bottom row) for second (P2; panels (a), (e)), third (P3; panels (b), (f)), fourth (P4; panels (c), (g)) precipitation quintiles, and all P (P2–P5 combined; panels (d), (h)) precipitation quintiles.

higher  $N$  subgroups (connected) than lower  $N$  subgroups (separated), with the caveat that area fractions of anvils and convective cores (rain areas) are not separated in this analysis. Because precipitation is nearly identical for all subgroups, at least, for P4 regime (Figure 5d), a larger cloud area fraction implies for a weaker precipitation efficiency associated with slightly higher SSTs of higher  $N$  subgroups (Figures 5e and 5f), which resembles convective-scale observations (Narney et al., 2019). Further discussion of precipitation efficiency is beyond the scope of this study.

### 3.3. Changes in Cloud Properties and Radiative Fluxes With $N$ as a Convective Aggregation Index

Next, we present the changes in cloud type-sorted cloud area fraction with the degree of convective aggregation by taking the differences between  $N = 1$  and  $N = 3$  (hereafter, referred to as subgroups 1–3) and between  $N = 2$  and  $N = 4^+$  subgroups (hereafter, referred to as subgroups 2–4+) for the P2, P3, P4 and combined precipitation (“All P”) regimes (Figure 6). The tendencies of change show decreases in the middle- and high-level clouds (up to  $-4\%$ ) but increases in the low-level clouds (up to  $2\%$ ). It is worth pointing out that increase of low-level clouds is smaller but reduction of high-level clouds is larger in P4 relative to P2. This result indicates that increase in low-level clouds is not due solely to reduction in high-level clouds. The most surprising result shown in Figure 6 is that the tendencies of change are nearly identical between the individual and combined precipitation regimes. This result suggests that partitioning into different precipitation regimes is not necessarily required to examine the tendencies of changes with the degree of convective aggregation. The tendencies are also nearly identical for subgroups 1–3 and 2–4+.

The similarity in the tendencies of cloud area fraction changes between the precipitation regimes and between subgroups 1–3 and 2–4+ is generally present in OLR (Figures 7a–7h) and to less extent in TOA albedo (Figures 7i–7p) for the majority of cloud types (A detailed discussion of the OLR and albedo tendencies will be given shortly.). The differences in magnitude between subgroups 1–3 and 2–4+ are, as expected, slightly reduced for the combined regimes, compared to those of the individual regimes. Note that TOA albedo is examined, instead of TOA SW, to eliminate the SW differences that can be caused by those in solar insolation of individual grids instead of changes in the degree of convective aggregation between subgroups.



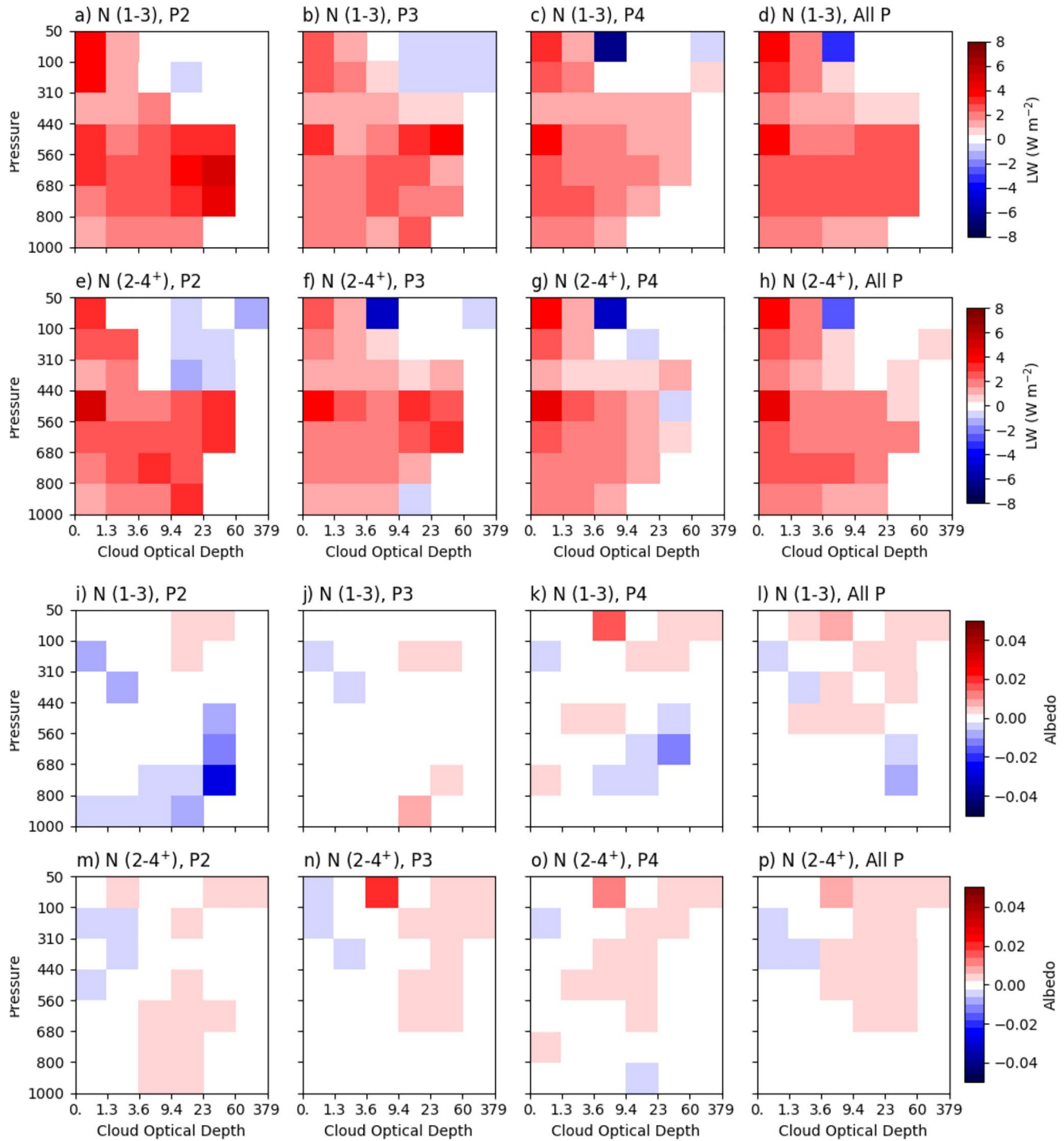


**Figure 7.** As in Figure 6, but for outgoing longwave radiative flux differences (a–h) and top-of-the-atmosphere albedo differences (i–p).

Previous studies (Tobin et al., 2012, 2013) showed that changes of the (clear and cloudy regions) averaged radiative fluxes with the degree of convective aggregation exhibit an increasing OLR and a decreasing TOA albedo, that is, an offset between LW and SW fluxes at TOA. The averaged radiative flux change ( $\Delta \bar{F}$ ) between two strengths of aggregation can be expressed as

$$\Delta \bar{F} = \Delta a (F_c - F_e) + a \Delta F_c + (1 - a) \Delta F_e \quad (1)$$

**Table 3**

*Decomposition of the Grid-Averaged Changes in Shortwave (SW) and Longwave (LW) Radiative Fluxes Between Two Subgroups (1–3 and 2–4+) Into Three Components and Their Sum for Different Precipitation Regimes: Cloud Radiative Effect Due To Change in Cloud Area Fraction, Change in Cloudy-Area Fluxes (Subscript c) and Change in Clear-Area Fluxes (Subscript e)*

	Subgroups	$\Delta(1 - a)$		$\Delta a (F_c - F_e)$	$a \Delta F_c$	$(1 - a) \Delta F_e$	Sum	Actual $\Delta \bar{F}$
All P regimes	1–3	–0.062	SW	–7.4	–5.4	0.0	–12.8	–12.8
			LW	8.7	4.3	0.6	13.6	13.8
	2–4+	–0.071	SW	–5.4	–6.5	0.0	–11.9	–11.9
			LW	8.4	4.8	0.6	13.8	14.3
P2 regime	1–3	–0.055	SW	–4.3	–7.9	–0.1	–12.3	–12.3
			LW	3.3	8.0	0.4	11.7	11.8
	2–4+	–0.089	SW	–7.3	–7.8	–0.1	–15.2	–15.2
			LW	5.9	9.6	0.5	16.0	15.9
P3 regime	1–3	–0.046	SW	–3.7	–5.3	–0.1	–9.1	–9.1
			LW	2.9	6.3	0.4	9.6	9.7
	2–4+	–0.060	SW	–5.1	–3.7	–0.1	–8.9	–8.8
			LW	4.2	5.9	0.4	10.5	11.3
P4 regime	1–3	–0.036	SW	–3.2	–6.1	0.0	–9.3	–9.4
			LW	2.6	6.5	0.4	9.5	9.6
	2–4+	–0.046	SW	–4.2	–4.0	0.0	–8.2	–8.0
			LW	3.3	6.2	0.4	9.9	10.1

*Note.* Change in clear-area fraction,  $\Delta(1 - a)$ , and actual grid-averaged flux changes between two subgroups are also shown.

where subscripts *c* and *e* denote cloudy and clear sky, respectively, and *a* is the cloud area fraction. The first term represents the cloud radiative effect resulted from change in cloud area fraction while the second and third terms represent radiative flux changes in the cloudy and clear sky, respectively. Part of the LW and SW sensitivity to the degree of convective aggregation is due to the increasing clear-sky area (Tobin et al., 2012, 2013), which corresponds to the first term in Equation (1). Tobin et al. (2013) showed a 0.05 albedo difference between the least to the most aggregated convective states, which translated to 20 W m<sup>–2</sup> for an incoming solar radiation of 400 W m<sup>–2</sup>. LW radiation escaping to space is increased by a similar amount. In the present analysis, changes in grid-averaged LW and SW for subgroups 1–3 and 2–4+ are slightly smaller for the combined regimes, ~–12 W m<sup>–2</sup> for SW and ~14 W m<sup>–2</sup> for LW, respectively (Table 3), which are partially related to smaller clear sky area increases from 3 to 1 (7.1%) and from 4+ to 2 (6.2%) subgroups. However, changes in cloudy-sky fluxes are equally or more important, particularly for LW (Table 3), if one accepts the simplification used in deriving Equation (1), which assumes uniform clouds.

How much do cloud type-sorted LW and SW fluxes change with the increasing degrees of convective aggregation (i.e., the decrease of *N*)? Are they quite different from one cloud type to another? The tendencies in LW changes (–1 to +1 W m<sup>–2</sup>) from moderately thick and thick anvil types are smaller than the rest of cloud types (Figures 7a–7h). The magnitude of LW changes from the rest of cloud types is between 2 and 8 W m<sup>–2</sup>, that is, emitting more infrared radiation to the space for lower *N* subgroups. These LW changes resemble those in cloud infrared emissivity for types with  $\tau \leq 30$  (Figures 8a–8h). The increased emission (Figures 7a–7h) could also be due to lower cloud tops for types with  $p_c \geq 440$  hPa (Figures 8i–8p). In contrast, most of 42 cloud types have the tendencies of changes in albedo hovered around 0, but the rest have the tendencies on an order of 0.01 (~2–4 W m<sup>–2</sup>) (Figures 7i–7p). The LW and albedo values for (9.4  $\geq \tau > 3.6$ , 100  $\geq p_c > 50$  hPa) cloud type are erroneously large, but this type does not contribute to the grid-averaged changes because of its small mean cloud fraction (Figures 3a, 3e and 4) and its change (Figure 6).

Is it possible to attribute the systematic trends in cloud area fraction, LW and albedo with the increase of *N* to the change of degrees of convective aggregation, not the differences in the environmental factors? PDFs of  $q_{v850}$ , precipitation rate, SST and  $\omega_{500}$  from the combined precipitation regimes (Figures 9a, 9e, 9i, and 9m) are

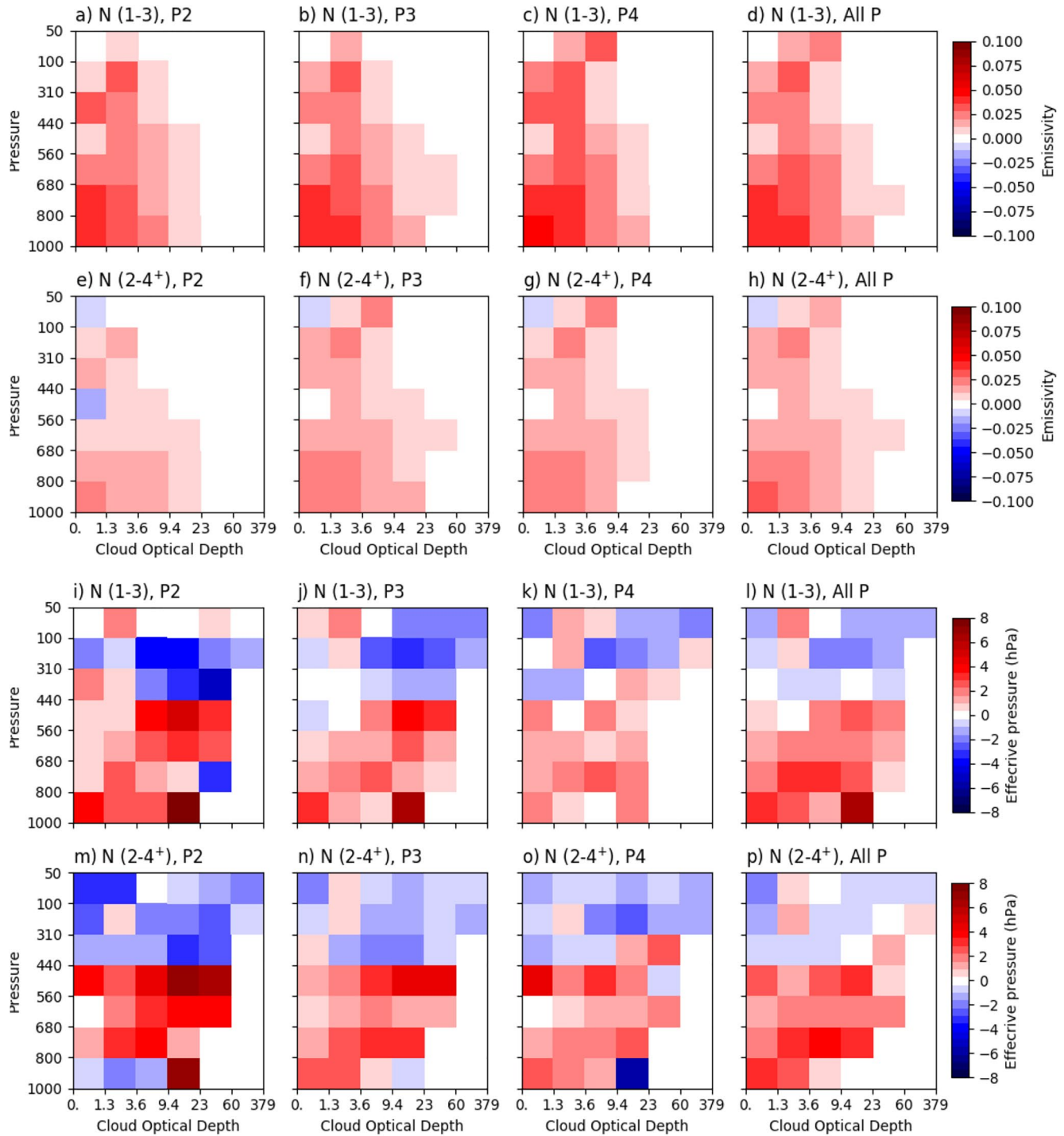


**Figure 8.** As in Figure 6, but for infrared emissivity differences (panels a–h) and cloud effective pressure differences (panels i–p).

compared with those from P2 and P4 regimes (Figure 5). PDFs of  $q_{v850}$  are significantly different among the subgroups from the combined regimes (Figure 9a), with the modes of the distribution differing by  $\sim 0.5 \text{ g kg}^{-1}$ . This result may suggest that there is a close association of drier atmospheres with lower  $N$  subgroups as the degree of convective aggregation increases, but this association is, at best, weaker for P2 and P4 regimes (Figures 5a and 5b), as in Tobin et al. (2012) but using relative humidity. There are also lower probability densities at the SST modes for lower  $N$  subgroups of the combined regimes (Figure 9i), but not for those of individual regimes (Figures 5e and 5f). Also, these SST differences between the subgroups are not as pronounced as those of  $q_{v850}$ .

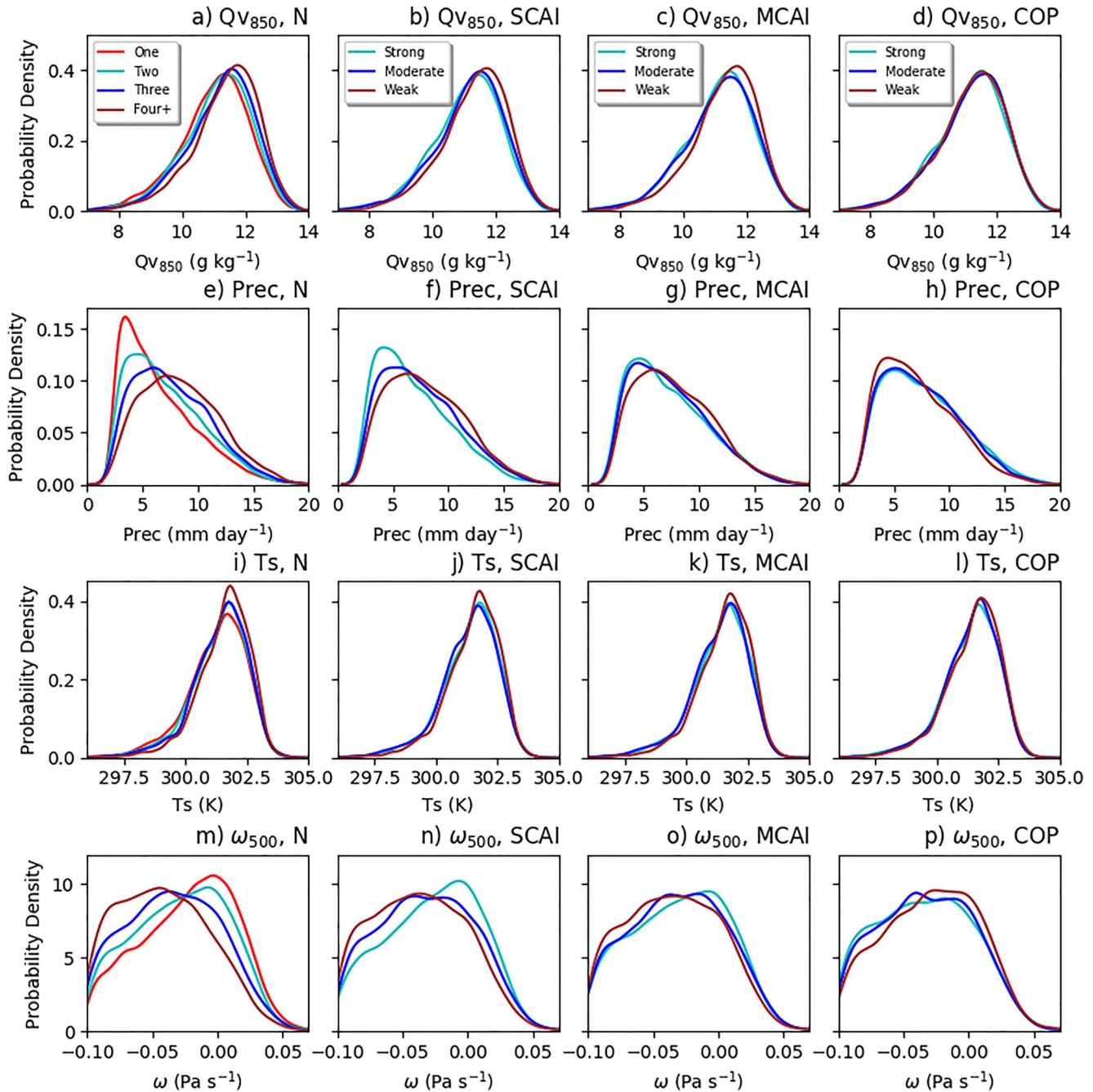


**Figure 9.** As in Figure 5, but for all (except for first quintile) precipitation regimes combined. The first column is for the four  $N$  subgroups while the last three columns are for terciles with weak (brown), moderate (blue) and strong (cyan) aggregation according to simple convective aggregation index (SCAI) (second column), modified SCAI (MCAI) (third column) and convective organization potential (COP) (right column).

The significant differences among  $N$  subgroups are evident in the PDFs of precipitation rate and  $\omega_{500}$  (Figures 9e and 9m). Both precipitation rate and  $\omega_{500}$  are significantly smaller for  $N = 1$  subgroup than those of multi-object subgroups, which is consistent with the findings of Tobin et al. (2012). This systematic trend can be explained by the proportion of data samples in each  $N$  subgroup from different precipitation regimes. Table 2 shows the number of data samples for each  $N$  subgroup that is decomposed by precipitation regimes. Proportions of data samples from lower precipitation regimes, which have smaller precipitation rate and smaller  $\omega_{500}$  (Figures 2a and 2d), increase as  $N$  decreases. For example, the proportion of P2 precipitation regime increases from 20.8% to 30.3% while that of P5 precipitation regime decreases from 40.3% to 10.8% as  $N$  decreases from  $4^+$  to 1, which



**Table 4**

*Proportion of Grids With 2, 3, and 4+ Cloud Objects Within a  $10^\circ \times 10^\circ$  Grid (N) for the Strong and Weak Terciles of SCAI, MCAI and COP*

	SCAI		MCAI		COP	
	Strong	Weak	Strong	Weak	Strong	Weak
$N = 2$	0.921	0.218	0.882	0.286	0.712	0.561
$N = 3$	0.078	0.334	0.113	0.308	0.230	0.244
$N = 4+$	0.001	0.448	0.005	0.406	0.058	0.196
Total number of grids	4,652	4,661	4,633	4,663	4,670	4,632

*Note.* The total number of data sample in each tercile is shown in the last row, which is used to obtain the fraction for each  $N$  subgroup.

explains the systematic variations of precipitation rate and  $\omega_{500}$  PDFs with  $N$  for the combined precipitation regimes (Figures 9e and 9m). These PDF differences for the combined precipitation regimes, rather than the changes in the degree of convective aggregation, can be ruled out as the likely reason for the changes seen in cloud fraction, LW and albedo with  $N$  as the corresponding PDF differences for individual precipitation regimes are much smaller (Figure 2). But the systematic trends in cloud area fraction, LW and albedo with the decrease of  $N$  are largely similar between the individual and combined precipitation regimes (Figures 6–8).

### 3.4. Changes in Cloud Properties and Radiative Fluxes With Morphology-Based Indices

Because different indices measure the degrees of convective aggregation differently, the same data samples may, as discussed in Section 2, not belong to the same strength category of different indices (Figure 1). We further quantify the characteristics of data samples in both weak and strong aggregation terciles, which can be helpful to explain changes in cloud properties and radiative fluxes with the strength of convective aggregation. We decompose strong and weak terciles by  $N$  in terms of proportion (Table 4) and average size of cloud objects (Table 5). The latter is measured by the number of footprints in cloud objects. The results are drastically different for SCAI, MCAI and COP. The strong SCAI tercile has 92% of  $N = 2$  grids but only 0.1% of  $N = 4+$  grids while the weak SCAI tercile has only 22% of  $N = 2$  grids but 45% of  $N = 4+$  grids, with small differences in the average size (16%–26% greater for strong tercile) except for  $N = 4+$  grids. Compared to SCAI, MCAI has slightly fewer  $N = 2$  grids in its strong tercile (88%) and more  $N = 2$  grids in its weak tercile (29%), but the average sizes are more than doubled for  $N = 2$  and  $N = 3$  subgroups from weak to strong terciles. On the other hand, proportions are comparable between the strong and weak COP terciles, that is, 71% versus 56% for  $N = 2$  grids, 23% versus 24% for  $N = 3$  grids. The averaged sizes of strong tercile are approximately three to four times larger than those of weak tercile. When  $N$  subgroups are combined, the average size decreases by 15% for SCAI, but increases by 42% for MCAI and 228% for COP from weak to strong terciles, respectively. The greater expansion of cloud object sizes with the degree of convective aggregation (COP/MCAI) can, as discussed below, impact the properties of optically-thick cloud types, which are mostly contributed by cloud object footprints.

It is expected that the three indices produce different results. Changes in cloud area fraction with the degree of convective aggregation are shown in Figures 10a–10c for the differences between two terciles with strong and weak degrees of convective aggregation according to SCAI, MCAI, and COP, respectively. Figure 10a shows

that the cloud area fraction changes from weak to strong aggregation for all cloud types using SCAI as a convective aggregation index are nearly identical to those using  $N$  as a convective aggregation index (Figure 6), which is also true for other variables (Figures 7 and 11). However, SCAI and COP exhibit contrasting changes from optically thin-to-moderate ( $\tau \leq 9.4$ ) low-level clouds (positive for SCAI, but negative for COP) and optically moderate-to-thick anvil ( $\tau > 3.6$ ) cloud types (negative for SCAI, but positive for COP). MCAI has small increase for optically thick anvil ( $\tau > 23$ ) cloud types. For the low-level cloud types, MCAI resembles SCAI with slightly smaller amount of increase. Therefore, the major difference between SCAI and MCAI appears in the sign of changes for optically-thick ( $\tau > 9.4$ ), high-level clouds. Area fractions of these cloud types increase as convective aggregation according to MCAI increases, but decrease according to SCAI,

**Table 5**

*Same as Table 4, but for Averaged Number of Footprints in Cloud Objects for the Strong and Weak Terciles of SCAI, MCAI and COP, Stratified by the Number of Cloud Objects Within a  $10^\circ \times 10^\circ$  Grid (N)*

	SCAI		MCAI		COP	
	Strong	Weak	Strong	Weak	Strong	Weak
$N = 2$	256	187	331	132	420	109
$N = 3$	373	310	533	227	580	153
$N = 4+$	1,111	376	1,185	352	678	232
All multi-object grids	266	313	358	251	472	144



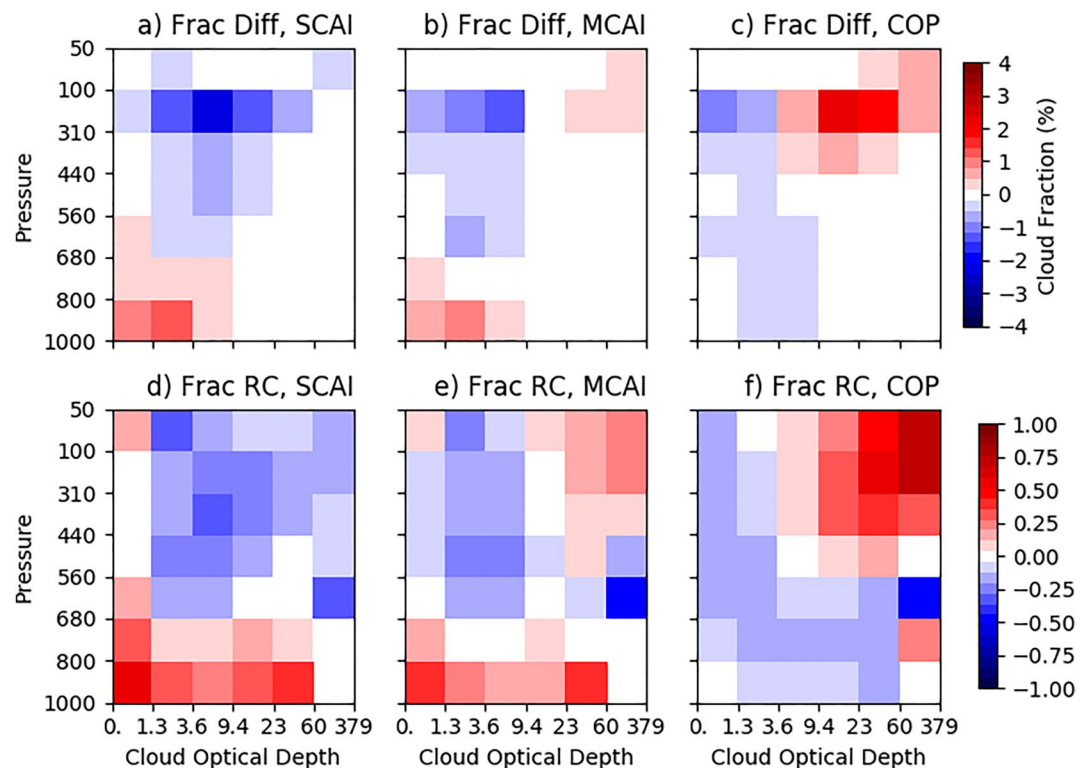


**Figure 10.** The mean cloud area fraction differences (top row) and relative changes with respect to the mean of the multi-object subset (bottom row) by  $p_c - \tau$  cloud types between high- and low-aggregation terciles according to convective aggregation measures: simple convective aggregation index (SCAI) (a), (d), modified SCAI (MCAI) (b), (e) and convective organization potential (COP) (c), (f).

related to the increase (decrease) of cloud object sizes as the strength of aggregation increases for MCAI (SCAI) discussed above.

To compare with previous studies, cloud types are merged over the entire range of  $\tau$  for two  $p_c$  intervals that represent low- and high-level clouds, respectively. Our findings agree with Tobin et al. (2013) and Stein et al. (2017) in that optically thin-to-moderate low-level clouds ( $p_c > 680$  hPa) increase with the degree of convective aggregation (3.6% for SCAI, 2.1% for MCAI), but decrease with increased organization potential (COP;  $-1.3\%$ ). Tobin et al. (2013) used brightness temperature ( $T_b$ ) to characterize clouds with different top heights. They showed that clouds with  $T_b > 285$  K (low-level clouds) increased with the degree of convective aggregation, which also included the increases in clear-sky area fraction. Our results indicate that clear sky area increases by 5.5% for SCAI and 2.3% for MCAI but decreases by 3.3% for COP, respectively. For reference, clear sky area differences are 6.2% and 7.1% for subgroups 1–3 and 2–4+ discussed in Section 3.3, respectively. Changes in the sum of clear-sky and low-level cloud area fractions are 9.1%, 4.4%, and  $-4.6\%$  for SCAI, MCAI, and COP, respectively.

The magnitudes of the changes in the high-level clouds are larger than those of the low-level clouds. The contrasting behaviors in the optically thin versus thick anvils distinguish both COP and MCAI from SCAI, due to the large contrasts in the averaged size of cloud objects between strong and weak COP terciles (Table 5). That is, the strong COP tercile includes much more optically moderate-to-thick clouds than MCAI and SCAI, which are contributed by cloud object footprints. As discussed in Section 3.1, the sum of anvil cloud types with  $310 \geq p_c > 100$  hPa is 33.2% for the entire multi-object subset. SCAI shows the change in the combined cloud types to be  $-5.5\%$  from weak to strong aggregation terciles compared to an increase of 3.9% for COP and a mild decrease of 2.1% for MCAI, respectively. So, the changes in fractions of high-level clouds from weak to strong aggregation are strongly dependent upon the proportion of  $N$  subgroup and averaged size of cloud objects within a  $10^\circ \times 10^\circ$  grid (Tables 4 and 5).

To determine the importance of changes for individual cloud types, we take the ratios of the changes shown in Figure 10a–10c to the means of the entire multi-object subset shown in Figure 3e. The results are shown in

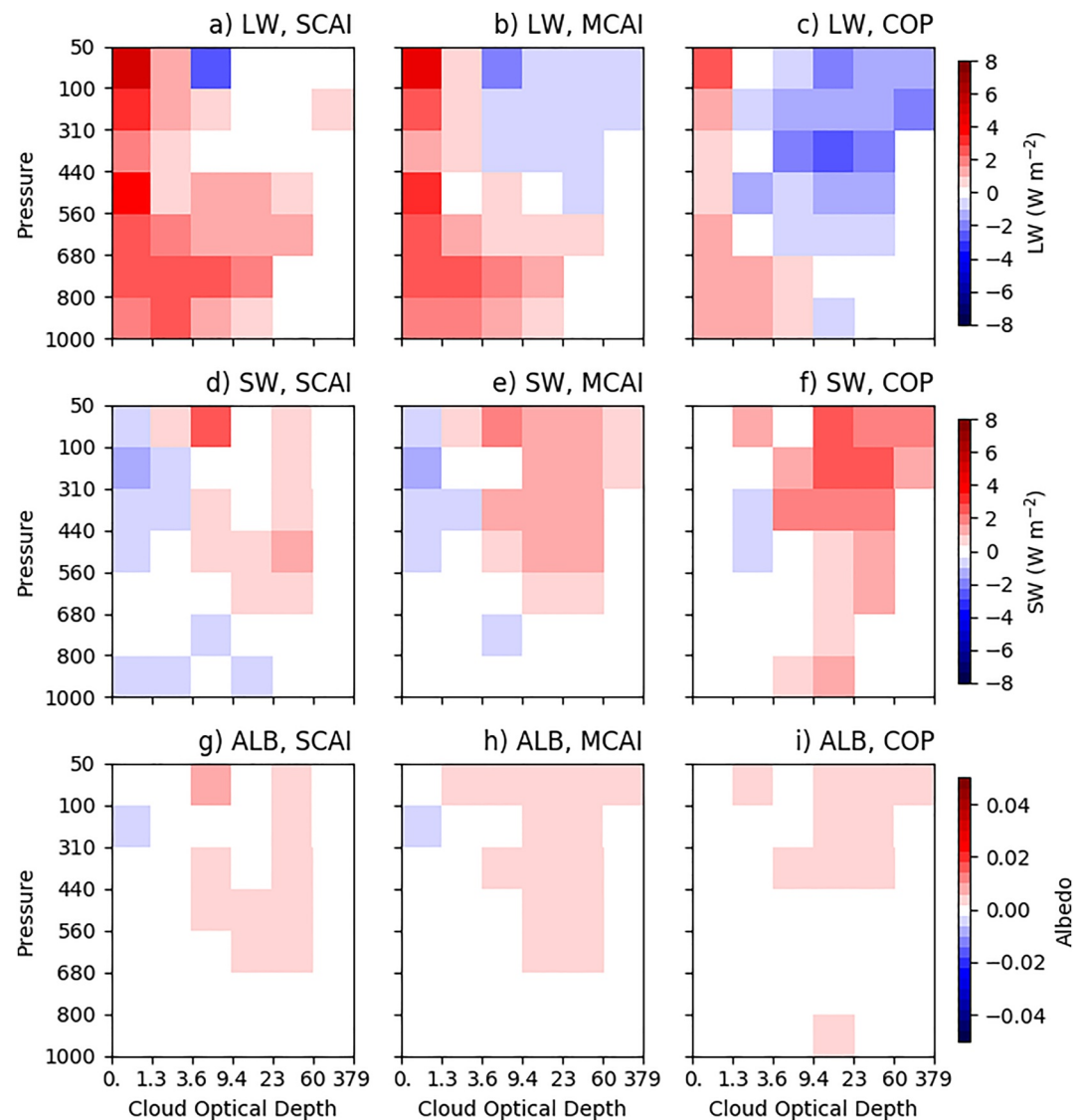


**Figure 11.** As in Figures 10a–10c, but for LW (top row), SW (middle row) and TOA albedo (bottom row) differences between the high- and low-aggregation terciles according to simple convective aggregation index (SCAI) (left column), modified SCAI (MCAI) (middle column) and convective organization potential (COP) (right column).

Figure 10d–10f for the three indices. The relative changes are in the range of 0.5–1 from some low-level cloud types with  $\tau \leq 60$  for SCAI/MCAI and optically-thick, high-level clouds for COP. The relative changes are  $\sim 0.25$  or greater for about a half of 42 cloud types. Therefore, changes from weak to strong aggregation strengths are significant for most cloud types. This illustrates the importance of examining individual cloud types, instead of more aggregated types, as discussed above, such as the upper-level anvils with a brightness temperature threshold used in previous studies (Pope et al., 2023; Tobin et al., 2012, 2013).

Figure 11 shows differences in cloud type-sorted LW flux, shortwave radiative flux and TOA albedo between strong and weak aggregation terciles for SCAI, MCAI and COP. For SCAI, the changes in these three qualities are similar to those using  $N$  as a convective aggregation index shown in Figure 7. However, there are also large differences in radiative fluxes for optically-thick, middle- and high-level cloud types among these three indices, in addition to their area fractions. Relative to their respective weak terciles, these clouds emit less infrared radiation and are more reflective for strong tercile of COP, to lesser extent, for strong tercile of MCAI, compared to strong tercile of SCAI. An explanation for this result is based upon the Xu et al. (2007) study. They showed that the PDFs of LW flux and albedo, constructed from footprint data, vary systematically with the size category of cloud objects. The large sizes

emit less infrared radiation and are more reflective relative to small sizes. As shown in Table 5, the differences in the average cloud-object size between strong and weak terciles are the largest for COP, followed by MCAI and SCAI.

A similar question as addressed in Section 3.3 can be asked again: Is it possible to attribute the systematic trends in cloud area fraction, LW and albedo to the change of degrees of convective aggregation, not the differences in the environmental factors? The last three columns of Figure 9 show PDFs of  $q_{v850}$ , precipitation rate, SST and  $\omega_{500}$  for weak, moderate and strong aggregation terciles of SCAI, MCAI and COP. As in Figure 9a, PDFs of  $q_{v850}$  for these terciles are not overlaid with each other when SCAI is used as an index (Figure 9b), compared to when COP is used as an index (Figure 9d); that is, there are shifts of PDFs toward smaller  $q_{v850}$  values as the degree of aggregation increases. When MCAI is used as an index, the curves are overlaid with each other for the moderate and strong aggregation terciles, but both are shifted away from that of the weak aggregation tercile (Figure 9c). On other hand, PDFs of  $q_{v850}$  are rather similar for all three terciles when COP is used as an index (Figure 9d).

When SCAI is used as an index, PDFs of  $\omega_{500}$  and precipitation rates show weaker ascent motion and weaker precipitation rates as the degree of convective aggregation increases (Figures 9f and 9n), which is similar to the results shown in Figures 9e and 9m except for using  $N$  as an index. However, separation of these PDFs among the three terciles is greatly reduced when either MCAI or COP is used as an index (Figures 9g, 9h, 9o, and 9p), suggesting for small differences in these environmental factors among the terciles. Lastly, the differences in PDFs of SST are also rather small among the three terciles of SCAI, MCAI, and COP (Figures 9j–9l). These small differences may justify our approach for not further partitioning the data into different SST regimes.

### 3.5. Sensitivity of Changes in Cloud Properties and Radiative Fluxes With Convective Aggregation to Large-Scale Dynamic Regimes

As mentioned in Section 2.3, we further stratify the data samples according to large-scale dynamic regimes with much narrower ranges of  $\omega_{500}$  variations. The data sample sizes for these two subsets are about 20% of the “full” data set (Table 1). The boundaries for dividing the data into three terciles were not changed.

Figure 12 shows the cloud area fraction and LW differences between the strong and weak aggregation terciles of the quasi-RCE (W0;  $|\omega_{500}| < 0.01 \text{ Pa s}^{-1}$ ) and the weak-ascending (W2;  $-0.03 < \omega_{500} \leq -0.01 \text{ Pa s}^{-1}$ ) dynamic regimes using SCAI, MCAI and COP as convective aggregation indices, similar to those shown in Figures 10a–10c and Figures 11a–11c for the wider range ( $-0.1 < \omega_{500} \leq 0.1 \text{ Pa s}^{-1}$ ) of dynamic regimes. Overall, the distinct results of the three indices as discussed in Section 3.4 are not sensitive to the dynamic regimes. Similar results are obtained for subgroups 1–3 and 2–4<sup>+</sup> (not shown), which are similar to those of SCAI (Figures 12a, 12d, 12g, and 12j). The magnitudes of the difference in cloud area fraction reduce slightly for some cloud types, such as optically thick, high-level clouds with COP as an index (Figures 12c and 12f), but those of LW can be larger or smaller. Nevertheless, the lack of strong sensitivity of changes to large-scale dynamic regimes suggests that further stratification of data set according to dynamic regimes is not needed to analyze the differences between two aggregation strengths and intercompare the performance of different aggregation indices. It further suggests that the manner cloud properties change and the underlying physical mechanism for aggregation might be similar under a fairly large range of dynamic conditions (i.e.,  $|\omega_{500}| < 0.1 \text{ Pa s}^{-1}$ ).

## 4. Summary and Discussions

From modeling studies, it is well established that cloud-radiation interactions are a critical mechanism for convective self-aggregation, especially the longwave radiative cooling of low clouds and environments (e.g., Pope et al., 2021, 2023; Wing et al., 2017). In this study, two data products from CERES observations combined with MERRA-2 reanalysis of large-scale dynamics and precipitation are used to understand the changes in cloud properties and radiative fluxes by cloud type with the degree of convective aggregation at the 1,000-km scale. The cloud types are represented by 42 bins of joint cloud optical depth ( $\tau$ ) and cloud top pressure ( $p_c$ ) distributions, following the ISCCP classification (Rossow & Schiffer, 1999). The degree of convective aggregation is characterized by either the number of cloud objects ( $N$ ) in a  $10^\circ \times 10^\circ$  grid or one of three morphology-based indices calculated with location, size and/or number of cloud objects within a  $10^\circ \times 10^\circ$  grid (Xu et al., 2019). For a given precipitation regime, we found that both middle- and high-level clouds increase but low-level clouds decrease as  $N$  increases. OLR decreases for most cloud types except for optically thick clouds and albedo also decreases for most cloud types except for optically thin clouds. These trends do not depend upon the precipitation or dynamic regime when the differences between two  $N$  subgroups are examined.

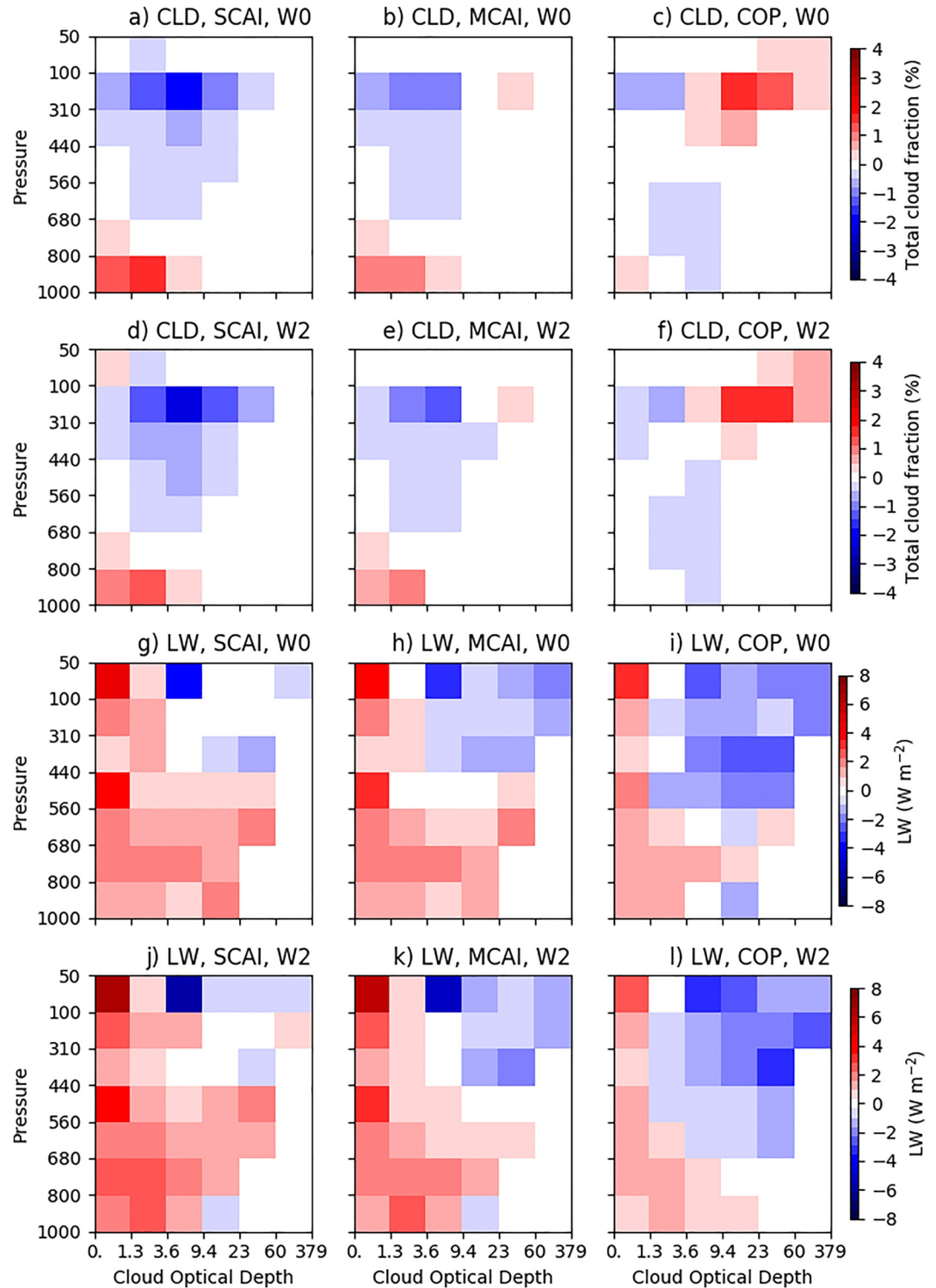


**Figure 12.** As in Figures 10a–10c, but for the W0 (a–c) and W2 (d–f) dynamic regimes. As in Figures 11a–11c, but for the W0 (g–i) and W2 (j–l) dynamic regimes, where dynamic regimes are defined as W2:  $-0.03 < \omega_{500} \leq -0.01 \text{ Pa s}^{-1}$ ; W0:  $|\omega_{500}| < 0.01 \text{ Pa s}^{-1}$ .

Three morphology-based convective aggregation indices (SCAI, MCAI, and COP) are used to divide the multi-object subset of data into three terciles with low, moderate and strong degrees of convective aggregation, respectively. The changes in cloud properties and radiative fluxes by cloud type with SCAI are similar to those of

using  $N$  as an index, agreeing with previous studies using grid-averaged properties (Tobin et al., 2012, 2013). For changes from weak to strong aggregation using  $N$  and SCAI as indices, area fractions of middle- and high-level cloud types decrease by up to 4% but that of low-level cloud types increase by up to 2%, and more infrared radiation is emitted to space ( $2\text{--}8\text{ W m}^{-2}$ ) from optically thin cloud types but more solar radiation is reflected ( $2\text{--}4\text{ W m}^{-2}$ ) from optically thick cloud types. Using COP, changes in area fractions of low- and high-level clouds and LW and albedo of optically moderate-to-thick clouds are substantially different from those obtained using SCAI, that is, high-level clouds increase up to 3% but low-level clouds decrease up to 1%, albedo increases slightly and LW decreases up to  $4\text{ W m}^{-2}$ . Changes associated with optically moderate-to-thick high-level cloud types are, however, smaller using MCAI than using COP while changes in low-level clouds and optically thin clouds with MCAI are consistent with those with SCAI. These differences among the three indices can be attributed to changes in the proportion of  $N$  subgroups and averaged size of cloud objects within a  $10^\circ \times 10^\circ$  grid from weak to strong terciles. The greater expansion of cloud object sizes for COP than for MCAI/SCAI contributes not only to the increase of the area fraction of optically-thick, middle- and high-level clouds, but also the decrease of their infrared radiation and the increase of their solar reflection as the degree of convective aggregation increases.

The changes in the sum of clear-sky and low-level cloud areas with the degrees of convective aggregation obtained using SCAI and MCAI, but not COP, agrees with prior studies (Tobin et al., 2012, 2013), which showed increases of these areas with the increase of convective aggregation. The weak increase of optically-thick, deep cloud types using MCAI may be more physical than the weak decrease of those cloud types using SCAI because convective aggregation enhances the intensity of active convective cores (Bretherton et al., 2005), but decreases the area fractions of other types of high-level clouds (Yuan & Houze, 2010). This assertion is based upon the fact that convective cores are well sampled by  $2\text{ km} \times 2\text{ km}$  resolution CERES MODIS data that are the basis of the FluxByCldTyp data (Eitzen et al., 2017; Sun et al., 2022), but further studies are needed to understand the physical mechanism.

Previous studies, except for Stein et al. (2017) using active-sensor observations, were unable to totally separate clear sky from cloudy sky and distinguish different cloud types because cloudy regions are defined by a threshold brightness temperature (Tobin et al., 2012, 2013) while the rest are composed of low-level clouds and truly clear region, which were regarded as environmental regions. They found that changes of the grid-averaged radiative fluxes with the degree of convective aggregation exhibit an increasing LW and a decreasing albedo at TOA, that is, an offset between LW and SW fluxes at TOA. Part of this sensitivity to the degree of convective aggregation is due to the increasing clear-sky area as convective aggregation increases, which increases cloud radiative effects (CREs) because cloudy regions emit much less infrared radiation and reflect much more solar radiation than clear regions. However, our analysis of the grid-averaged radiative fluxes also suggest that changes in cloudy-sky fluxes are equally or more important, particularly for LW, than the CREs due to change in clear-sky area fraction. The changes in cloudy-sky fluxes from weak and strong aggregation strengths vary greatly with cloud type and are due primarily to the change in the degree of convective aggregation, but less to changes in the environmental factors.

The results from the analysis of dynamic regime sensitivity indicate that the differences between the strong and weak aggregation subgroups/terciles of narrow dynamic regimes, including a regime that is closest to the RCE condition, are nearly identical to those of the wider range ( $|\omega_{500}| < 0.1\text{ Pa s}^{-1}$ ) of dynamic regimes when either  $N$ , SCAI, MCAI, or COP is used as a convective aggregation index. That is, the distinct behaviors of the four indices are not changed at all as the dynamic range is narrowed. The magnitudes of the differences in cloud area fraction are reduced slightly, however. We acknowledge that large-scale dynamics play a significant role in determining area fractions of different cloud types and surface precipitation for a given aggregation state, which also affects precipitation efficiency (Lutsko & Cronin, 2018; Narsey et al., 2019). The analysis of external forcing factors for contributing to these differences between two averaged aggregation strengths does not reveal that large-scale dynamics regimes play a significant role in our results. Changes in the degree of convective aggregation seem to be the primary reason although none of the indices may be able to accurately depict the convective aggregation strengths.

Finally, it should be pointed out that the simulated clear sky fractions in CRMs and GCMs under RCE are much greater than those of the dataset used in this study. For example, they are 27.8% and 22.8% for single- and multi-object subsets, respectively (Section 3.1), compared to 50%–80% in RCE simulations (Pope et al., 2023), which also exhibit clearly defined convective lifecycle. However, the observed convective systems in different



aggregation stages could coexist in an area of  $10^\circ \times 10^\circ$  and the morphology-based indices might not adequately represent the true degrees of convective aggregation (e.g., due to missing small convective cells). It should be pointed out that these small clear sky fractions are typical of the deep tropics with active convection (e.g., Tobin et al., 2013). In other words, changes of clear sky fraction and low-tropospheric moisture with the degree of convective aggregation presented in this analysis are not comparable to what models simulate under the RCE condition with small domains. To what degree are physical mechanisms behind the observed convective aggregation, which cannot be untangled in this study, similar to those in CRM studies is unknown although there are similarities in the changes of cloud area fraction and radiative properties with the degree convective aggregation. These similarities may point to the relevance of observed aggregation to convective self-aggregation in models, as in earlier studies. It is possible to select small subsets of cases with large clear sky fractions for a more in-depth analysis, which is, however, beyond the scope of this study.

## Data Availability Statement

The cloud object data can be downloaded from <https://cloud-object.larc.nasa.gov>. The CERES FluxByCldTyp (FBCT) level-3 data product can be accessed via CERES data portal (<https://ceres.larc.nasa.gov/data/>). The MERRA2 data (accessed at <https://disc.gsfc.nasa.gov/datasets?project=MERRA-2>) are available from NASA Global Modeling and Assimilation Office (GMAO). Omega500 is obtained from MERRA-2 tavg1\_2d\_slv\_Nx: 2d,1-Hourly,Time-Averaged,Single-Level,Assimilation,Single-Level Diagnostics V5.12.4 (M2T1NX-SLV), doi: [10.5067/VJAFPLIICSIV](https://doi.org/10.5067/VJAFPLIICSIV); Precipitation (prectot) is obtained from MERRA-2 tavgU\_2d\_flg\_Nx: 2d,diurnal,Time-Averaged,Single-Level,Assimilation, Surface Flux Diagnostics V5.12.4 (M2TUNXFLX), doi: [10.5067/7MCPBJ41Y0K6](https://doi.org/10.5067/7MCPBJ41Y0K6).

## Acknowledgments

This work has been supported by NASA Science of Terra, Aqua, and NPP program (KX and YZ) and the NASA CERES project (MS and SK). The authors would like to thank three anonymous reviewers for their constructive comments.

## References

- Arnold, N. P., & Randall, D. A. (2015). Global-scale convective aggregation: Implications for the Madden-Julian oscillation. *Journal of Advances in Modeling Earth Systems*, 7(4), 1499–1518. <https://doi.org/10.1002/2015MS000498>
- Bao, J., Sherwood, S. C., Colin, M., & Dixit, V. (2017). The robust relationship between extreme precipitation and convective organization in idealized numerical modeling simulations. *Journal of Advances in Modeling Earth Systems*, 9(6), 2291–2303. <https://doi.org/10.1002/2017MS001125>
- Bony, S., Semie, A., Kramer, R. J., Soden, B., Tompkins, A. M., & Emanuel, K. A. (2020). Observed modulation of the tropical radiation budget by deep convective organization and lower-tropospheric stability. *AGU Advances*, 1(3), e2019AV000155. <https://doi.org/10.1029/2019AV000155>
- Bretherton, C. S., Blossey, P., & Khairoutdinov, M. (2005). An energy-balance analysis of deep convective self-aggregation above uniform SST. *Journal of the Atmospheric Sciences*, 62(12), 4273–4292. <https://doi.org/10.1175/jas3614.1>
- Coppin, D., & Bony, S. (2015). Physical mechanisms controlling the initiation of convective self-aggregation in a general circulation model. *Journal of Advances in Modeling Earth Systems*, 7(4), 2060–2078. <https://doi.org/10.1002/2015ms000571>
- Eitzen, Z. A., Su, W., Xu, K.-M., Loeb, N., Sun, M., Doelling, D. R., et al. (2017). Evaluation of a general circulation model by the CERES Flux-by-Cloud Type simulator. *Journal of Geophysical Research: Atmospheres*, 122, 10655–10668. <https://doi.org/10.1002/2017JD027076>
- Gelaro, R., McCarty, W., Suárez, M. J., Todling, R., Molod, A., Takacs, L., et al. (2017). The modern-Era Retrospective analysis for Research and Applications, version 2 (MERRA-2). *Journal of Climate*, 30(14), 5419–5454. <https://doi.org/10.1175/JCLI-D-16-0758.1>
- Green, R., & Wielicki, B. A. (1997). Convolution of imager cloud properties with CERES footprint point spread function. *CERES Algorithm Theoretical Basis Doc. 4.4*. Retrieved from [http://ceres.larc.nasa.gov/documents/ATBD/pdf/r2\\_2/ceres-atbd2.2-s4.4.pdf](http://ceres.larc.nasa.gov/documents/ATBD/pdf/r2_2/ceres-atbd2.2-s4.4.pdf)
- Held, I. M., Hemler, R. S., & Ramaswamy, V. (1993). Radiative-convective equilibrium with explicit two-dimensional moist convection. *Journal of the Atmospheric Sciences*, 50(23), 3909–3927. [https://doi.org/10.1175/1520-0469\(1993\)050<3909:rcewet>2.0.co;2](https://doi.org/10.1175/1520-0469(1993)050<3909:rcewet>2.0.co;2)
- Holloway, C. E., Wing, A. A., Bony, S., Muller, C., Masunaga, H., L'Ecuyer, T. S., et al. (2017). Observing convective aggregation. *Surveys in Geophysics*, 38(6), 1199–1236. <https://doi.org/10.1007/s10712-017-9419-1>
- Jakob, C., Singh, M. S., & Jungandreas, L. (2019). Radiative convective equilibrium and organized convection: An observational perspective. *Journal of Geophysical Research: Atmospheres*, 124(10), 5418–5430. <https://doi.org/10.1029/2018JD030092>
- Kadoya, T., & Masunaga, H. (2018). New observational metrics of convective self-aggregation: Methodology and a case study. *Journal of Meteorology Society Japan*, 96(6), 535–548. <https://doi.org/10.2151/jmsj.2018-054>
- Lebsock, M. D., L'Ecuyer, T. S., & Pincus, R. (2017). An observational view of relationships between moisture aggregation, cloud, and radiative heating profiles. *Surveys in Geophysics*, 38(6), 1237–1254. <https://doi.org/10.1007/s10712-017-9443-1>
- Loeb, N. G., Manalo-Smith, N., Kato, S., Miller, W. F., Gupta, S. K., Minnis, P., & Wielicki, B. A. (2003). Angular distribution models for top-of-atmosphere radiative flux estimation from the clouds and the Earth's radiant energy system instrument on the tropical rainfall measuring mission satellite. Part I: Methodology. *Journal of Applied Meteorology*, 42(2), 240–265. [https://doi.org/10.1175/1520-0450\(2003\)042<0240:admfto>2.0.co;2](https://doi.org/10.1175/1520-0450(2003)042<0240:admfto>2.0.co;2)
- Lutsko, N. J., & Cronin, T. W. (2018). Increase in precipitation efficiency with surface warming in radiative-convective equilibrium. *Journal of Advances in Modeling Earth Systems*, 10(11), 2992–3010. <https://doi.org/10.1029/2018MS001482>
- Mapes, B. E. (1993). Gregarious tropical convection. *Journal of the Atmospheric Sciences*, 50(13), 2026–2037. [https://doi.org/10.1175/1520-0469\(1993\)050<2026:gtrc>2.0.co;2](https://doi.org/10.1175/1520-0469(1993)050<2026:gtrc>2.0.co;2)
- Masunaga, H., Holloway, C. E., Kanamori, H., Bony, S., & Stein, T. H. M. (2021). Transient aggregation of convection: Observed behavior and underlying processes. *Journal of Climate*, 34(5), 1685–1700. <https://doi.org/10.1175/JCLI-D-19-0933.1>
- Minnis, P., Garber, D. P., Young, D. F., Arduini, R. F., & Takano, Y. (1998). Parameterizations of reflectance and effective emittance for satellite remote sensing of cloud properties. *Journal of the Atmospheric Sciences*, 55(22), 3313–3339. [https://doi.org/10.1175/1520-0469\(1998\)055<3313:porace>2.0.co;2](https://doi.org/10.1175/1520-0469(1998)055<3313:porace>2.0.co;2)

- Minnis, P., Sun-Mack, S., Young, D. F., Heck, P. W., Garber, D. P., Chen, Y., et al. (2020). CERES MODIS cloud product retrievals for edition 4—Part I: Algorithm changes. *IEEE Transactions of Geoscience Remote Sensing*. <https://doi.org/10.1109/TGRS.2020.3008866>
- Minnis, P., Sun-Mack, S., Young, D. F., Heck, P. W., Garber, D. P., Chen, Y., et al. (2011). CERES Edition-2 cloud property retrievals using TRMM VIRS and Terra and Aqua MODIS data—Part I: Algorithms. *IEEE Transactions of Geoscience Remote Sensing*, 49(11), 4374–4400. <https://doi.org/10.1109/TGRS.2011.2144601>
- Muller, C. J., & Bony, S. (2015). What favors convective aggregation and why? *Geophysical Research Letters*, 42(13), 5626–5634. <https://doi.org/10.1002/2015GL064260>
- Muller, C. J., & Held, I. M. (2012). Detailed investigation of the self-aggregation of convection in cloud resolving simulations. *Journal of the Atmospheric Sciences*, 69(8), 2551–2565. <https://doi.org/10.1175/JAS-D-11-0257.1>
- Muller, C. J., Yang, D., Craig, G., Cronin, T., Fildier, B., Haerter, J. O., et al. (2022). Spontaneous aggregation of convective storms. *Annual Review of Fluid Mechanics*, 54(1), 133–157. <https://doi.org/10.1146/annurev-fluid-022421-011319>
- Nakazawa, T. (1988). Tropical super clusters within intraseasonal variations over the western Pacific. *Journal of Meteorology Society of Japan*, 66(6), 823–839. [https://doi.org/10.2151/jmsj1965.66.6\\_823](https://doi.org/10.2151/jmsj1965.66.6_823)
- Narsey, S., Jakob, C. N., Singh, M. S., Bergemann, M., Louf, V., Protat, A., & Williams, C. (2019). Convective precipitation efficiency observed in the tropics. *Geophysical Research Letters*, 46(22), 13574–13583. <https://doi.org/10.1029/2019GL085031>
- Pope, K. N., Holloway, C. E., Jones, T. R., & Stein, T. H. M. (2021). Cloud-radiation interactions and their contributions to convective self-aggregation. *Journal of Advances in Modeling Earth Systems*, 13(9), e2021MS002535. <https://doi.org/10.1029/2021MS002535>
- Pope, K. N., Holloway, C. E., Jones, T. R., & Stein, T. H. M. (2023). Radiation, clouds, and self-aggregation in RCEMIP simulations. *Journal of Advances in Modeling Earth Systems*, 15(2), e2022MS003317. <https://doi.org/10.1029/2022MS003317>
- Rienecker, M. M., Suarez, M. J., Gelaro, R., Todling, R., Bacmeister, J., Liu, E., et al. (2011). MERRA: NASA's modern-era retrospective analysis for research and applications. *Journal of Climate*, 24(14), 3624–3648. <https://doi.org/10.1175/JCLI-D-11-00015.1>
- Rossow, W. B., & Schiffer, R. A. (1999). Advances in understanding clouds from ISCCP. *Bulletin of American Meteorological Society*, 80(11), 2261–2287. [https://doi.org/10.1175/1520-0477\(1999\)080<2261:aicufi>2.0.co;2](https://doi.org/10.1175/1520-0477(1999)080<2261:aicufi>2.0.co;2)
- Stein, T. H. M., Holloway, C. E., Tobin, I., & Bony, S. (2017). Observed relationships between cloud vertical structure and convective aggregation over tropical ocean. *Journal of Climate*, 30(6), 2187–2207. <https://doi.org/10.1175/JCLI-D-16-0125.1>
- Sun, M., Doelling, D. R., Loeb, N. G., Scott, R. C., Wilkins, J., Nguyen, L. T., & Mlynarczyk, P. (2022). Clouds and the Earth's radiant energy system (CERES) FluxByCldTyp edition 4 data product. *Journal of Atmospheric and Oceanic Technology*, 39(3), 303–318. <https://doi.org/10.1175/JTECH-D-21-0029.1>
- Tobin, I., Bony, S., Holloway, C. E., Grandpeix, J. Y., Se`ze, G., Coppin, D., et al. (2013). Does convective aggregation need to be represented in cumulus parameterizations? *Journal of Advances in Modeling Earth Systems*, 5(4), 692–703. <https://doi.org/10.1002/jame.20047>
- Tobin, I., Bony, S., & Roca, R. (2012). Observational evidence for relationships between the degree of aggregation of deep convection, water vapor, surface fluxes, and radiation. *Journal of Climate*, 25(20), 6885–6904. <https://doi.org/10.1175/JCLI-D-11-00258.1>
- Tompkins, A. M., & Semie, A. G. (2017). Organization of tropical convection in low vertical wind shears: Role of updraft entrainment. *Journal of Advances in Modeling Earth Systems*, 9(2), 1046–1068. <https://doi.org/10.1002/2016MS000802>
- White, B., Buchanan, A., Birch, C., Stier, P., & Pearson, K. (2018). Quantifying the effects of horizontal grid length and parameterized convection on the degree of convective organization using a metric of the potential for convective interaction. *Journal of the Atmospheric Sciences*, 75(2), 425–450. <https://doi.org/10.1175/jas-d-16-0307.1>
- Wing, A. A., & Emanuel, K. A. (2014). Physical mechanisms controlling self-aggregation of convection in idealized numerical modeling simulations. *Journal of Advances in Modeling Earth Systems*, 6(1), 59–74. <https://doi.org/10.1002/2013ms000269>
- Wing, A. A., Emanuel, K. A., Holloway, C. E., & Muller, C. (2017). Convective self-aggregation in numerical simulations: A review. *Surveys in Geophysics*, 38(6), 1173–1197. <https://doi.org/10.1007/s10712-017-9408-4>
- Xu, K.-M., Hu, Y., & Wong, T. (2019). Convective aggregation and indices examined from CERES cloud object data. *Journal of Geophysical Research*, 124(24), 13604–13624. <https://doi.org/10.1029/2019JD030816>
- Xu, K.-M., Wong, T., Dong, S., Chen, F., Kato, S., & Taylor, P. C. (2016). Cloud object analysis of CERES Aqua observations of tropical and subtropical cloud regimes: Four-year climatology. *Journal of Climate*, 29(5), 1627–1638. <https://doi.org/10.1175/JCLI-D-14-00836.1>
- Xu, K.-M., Wong, T., Dong, S., Chen, F., Kato, S., & Taylor, P. C. (2017). Cloud object analysis of CERES Aqua observations of tropical and subtropical cloud regimes: Evolution of cloud object size distribution during the Madden-Julian Oscillation. *Journal of Quantitative Spectroscopy and Radiative Transfer*, 188, 148–158. <https://doi.org/10.1016/j.jqsrt.2016.06.008>
- Xu, K.-M., Wong, T., Wielicki, B. A., & Parker, L. (2008). Statistical analyses of satellite cloud object data from CERES. Part IV: Boundary-layer cloud object during 1998 El Nino. *Journal of Climate*, 21(7), 1500–1521. <https://doi.org/10.1175/2007jcli1710.1>
- Xu, K.-M., Wong, T., Wielicki, B. A., Parker, L., & Eitzen, Z. A. (2005). Statistical analyses of satellite cloud object data from CERES. Part I: Methodology and preliminary results of 1998 El Nino/2000 La Nina. *Journal of Climate*, 18(13), 2497–2514. <https://doi.org/10.1175/jcli3418.1>
- Xu, K.-M., Wong, T., Wielicki, B. A., Parker, L., Lin, B., Eitzen, Z. A., & Branson, M. (2007). Statistical analyses of satellite cloud object data from CERES. Part II: Tropical convective cloud objects during 1998 El Nino and evidence for supporting the fixed anvil temperature hypothesis. *Journal of Climate*, 20(5), 819–842. <https://doi.org/10.1175/jcli4069.1>
- Yuan, J., & Houze, R. A., Jr. (2010). Global variability of mesoscale convective system anvil structure from A-Train satellite data. *Journal of Climate*, 23(21), 5864–5888. <https://doi.org/10.1175/2010JCLI3671.1>
- Zeng, X. (2023). Atmospheric instability and its associated oscillations in the tropics. *Atmosphere*, 14(3), 433. <https://doi.org/10.3390/atmos14030433>